

**MEASUREMENT OF A 3D COIL APPLIED TO  
UNDERWATER MAGNETO-INDUCTIVE COMMUNICATION**

by

Sri Raghu Padyath Ravindran

Submitted in partial fulfilment of the requirements  
for the degree of Master of Applied Science

at

Dalhousie University  
Halifax, Nova Scotia  
November 2018

**To my lovely parents Mr. Padyath Ravindran and  
Mrs. Geetha Ravindran**

# TABLE OF CONTENTS

<b>LIST OF TABLES</b> .....	v
<b>LIST OF FIGURES</b> .....	vi
<b>LIST OF ABBREVIATIONS AND SYMBOLS USED</b> .....	viii
<b>ACKNOWLEDGMENTS</b> .....	xi
<b>ABSTRACT</b> .....	xii
<b>CHAPTER 1 INTRODUCTION</b> .....	1
1.1 BACKGROUND.....	1
1.2 THESIS OVERVIEW .....	6
1.3 ORGANIZATION OF THE THESIS .....	8
<b>CHAPTER 2 MAGNETO INDUCTIVE COMMUNICATION SYSTEM</b> .....	9
2.1 CONCEPT OF MI SYSTEM.....	9
2.2 STATE-OF-ART.....	10
2.3 MI SYSTEM DESCRIPTION .....	13
2.3.1 Magnetic Transmission.....	13
2.3.3 Loss in Seawater .....	23
2.4 FREQUENCY DEPENDENT NOISE: .....	24
2.5 OPTIMUM FREQUENCY SELECTION .....	27
<b>CHAPTER 3 MULTI-COIL IMPLEMENTATION</b> .....	32
3.1 EARLY PROTOTYPES .....	32
3.1.1 Single Coil Setup.....	32
3.1.2 Digital Modem interface.....	37
3.2 TRANSMITTER FRONT-END DESIGN .....	40
3.3 ENCASING THE 3D COIL.....	43

3.4	MAGNETO INDUCTIVE RECEIVER: .....	46
<b>CHAPTER 4 MEASUREMENTS.....</b>		<b>50</b>
4.1	TEST TANK TRIAL .....	50
4.2	EXPERIMENTAL RESULTS.....	57
4.2.1	Noise Analysis.....	57
4.2.2	Single Coil Response.....	58
4.2.3	Multiple Coil Response .....	62
<b>CHAPTER 5 CONCLUSION.....</b>		<b>64</b>
5.1	RESULTS.....	64
5.2	DISCUSSION ON FUTURE WORKS.....	65
<b>APPENDIX A COILS COLOR SCHEMA .....</b>		<b>66</b>
<b>APPENDIX B COIL ENCLOSURE DESIGN.....</b>		<b>67</b>
<b>APPENDIX C TRANSMITTER BEAMFORMING ANGLES.....</b>		<b>70</b>
<b>APPENDIX D DIGITAL MODEM .....</b>		<b>72</b>
<b>BIBLIOGRAPHY.....</b>		<b>75</b>

## LIST OF TABLES

Table 1: Environment impacts over different underwater communications [1].....	2
Table 2: Comparison merits of different underwater communications [1] .....	5
Table 3: Components lists used to implement MI single coil transceiver set up .....	33
Table 4: Aquatron Tank Facility Specifications.....	51
Table 5: Multi coil set up - Transmitter components list.....	54

## LIST OF FIGURES

Figure 1: Proposed AC DC Converter .....	9
Figure 2 : Schematic block represents MI coupling .....	11
Figure 3: Magnetic flux density representation for current in a coil .....	14
Figure 4 :Magnetic flux $\Phi_{11}$ , $\Phi_{12}$ generated by current $i_1$ .....	14
Figure 5: Transformer model MI transceiver.....	16
Figure 6 : MI transformer model to equivalent two - port network [11].....	17
Figure 7: Measured atmospheric noise .....	27
Figure 8: Communication bandwidth (identified by squares) and distance (identified by circles) vs. carrier frequency for different number of turns.....	29
Figure 9: Capacity contour plot as a function of Frequency with Distance .....	30
Figure 10: Single coil architecture of initial MI system.....	32
Figure 11: Path loss vs distance at 1 MHz.....	34
Figure 12: Path loss vs distance at 22.5 kHz .....	34
Figure 13: Graph shows the scatter plot of received and equalized signal [11] .....	35
Figure 14: Prototype testing phase .....	36
Figure 15: Prototype display at Dalhousie's event .....	36
Figure 16: FSK signal shows two frequency of transmission .....	37
Figure 17: Circuit schematic of a digital Transceiver set up using ADS tool .....	39
Figure 18: Sinusoidal input of 80Khz frequency, $2.5V_{pp}$ .....	39
Figure 19: Square input of 80Khz frequency, $2.5V_{high}$ (no sweep) .....	39
Figure 20: Square input of 80 KHz frequency, $2.5V_{high}$ (with parametric sweep) .....	40
Figure 21: Block representation of implemented multi-coil setup .....	41

Figure 22 : Inductance plot for multi-coil transmitter .....	43
Figure 23: 3-element coil windings and 3D printed casing.....	44
Figure 24: Coil color and channel orientation .....	45
Figure 25: Adding connector cables and sealing with epoxy .....	46
Figure 26: Sealed receiver coil facing enclosed transmitter.....	46
Figure 27: Schematic layout for underwater testing.....	50
Figure 28: Transmitter signal processing set up.....	52
Figure 29: Transmitter and Receiver were deployed underwater.....	55
Figure 30: Measured noise at different gain levels.....	58
Figure 31: Measured Gain as a function of Frequency and Distance.....	59
Figure 32: Comparison of Path Loss in Seawater and Air at 2m and 3m distances.....	60
Figure 33: Comparison of Measured gain and Simulated gain as a function frequency for different distances .....	61
Figure 34: Comparison of Measured gain and Analytical gain as a function of Angle at 2meters distance for the multiple coil.....	62
Figure 35: Pathloss as a Function of Angle for multiple channels.....	63

# LIST OF ABBREVIATIONS AND SYMBOLS USED

## ABBREVIATIONS

MI	Magneto – Inductive
WPT	Wireless Power Transfer
AUVs	Autonomous Underwater Vehicle
MIC	Magnetic Inductive Coupling
EM	Electro Magnetic
WSN	Wireless Sensor Network
UWSN	Underwater Wireless Sensor Network
dB	decibel
dBm	decibel – milliwatts
SNR	signal to noise ratio
ROV	Remotely Operated Underwater Vehicle
EVM	Evaluation Module
PA	Power Amplifier
AC	Alternating Current
DC	Direct Current
RF	Radio Frequency
DAQ	Data Acquisition
MODEM	Modulator Demodulator
USB	Universal Serial Bus
AWG	American Wire Gauge

LNA	Low Noise Amplifier
IOT	Internet of Things
SPDIF	Sony Philips Digital Interface Format
ESC	External Sound Card
DAC	Data Acquisition Card
PSD	Power Spectral Density
BTL	Bridged – Tied Load

## SYMBOLS

$\mu$	Magnetic permeability
$\mu_r$	Relative permeability
$\mu_0$	Magnetic permeability of free space
$\omega_{res}$	Angular frequency, $[2\pi f_{res}]$
$f_{res}$	Resonant frequency
$\Phi$	Magnetic flux density
$\alpha$	Angle of arrival of signal
$\lambda$	Wavelength
$\sigma$	Electrical conductivity
$\epsilon$	Dielectric constant or Electrical permittivity
$\epsilon_0$	Electrical permittivity of free space
$\epsilon_r$	Relative permittivity
$\phi_r$	Merit factor aperture

B	Magnetic field strength
$w$	Channel bandwidth
$F_a$	Atmospheric noise temperature
$F_k$	Atmospheric noise
k	Boltzmann constant [ $1.380649 \times 10^{-23} \text{ Jk}^{-1}$ ]
$k_o$	wave number for free space
$T_o$	Receiver temperature
$Z_o$	Wave impedance of free space, $Z_o = \sqrt{\frac{\mu_o}{\epsilon_o}}$

## **ACKNOWLEDGMENTS**

Foremost, I would like to thank my supervisor Dr. Jean – François Bousquet for his guidance and continuous support to take the research to the next level. His patience and experience helped to steer whenever I needed guidance. The learning I have done in the lab throughout this process is invaluable and shaped me a better student and researcher because of it. I also would like to thank Dr. Vincent Sieben and Dr. William Phillips to participate in my supervisory committee.

To all the individuals at Dalhousie university who were there when I had questions and concerns or just needed to talk to someone Nicole, Mark, Taylor, Jordan, Rebecca – I cannot thank you enough. All the people who spent their valuable time, I can't name you all but thank you all for keeping me on track.

Last, but not least, thank you to my ever-loving family. I really would not have been able to do any of this without your unconditional love and support, even from other side of the world. Amma, Appa, I love you so much and thank you for all you do putting up with me. Your encouragement helped me every day. None of this would have been possible without you both!

Thank you all...

## **ABSTRACT**

In this work, a magneto-inductive (MI) communication link is characterized using a compact three-dimensional transmitter front end. A realistic model of the MI link that includes the effect of coupling loss, conductive loss, as well as atmospheric noise is validated using measurements in a seawater tank. A relatively high capacity on the order of 100 kbps can be achieved for a distance less than approximately 4 meters. The magneto-inductive link channel gain is measured as a function of distance and frequency. This is realized with a modest power consumption below 0.1 W at the transmitter, and for small coil dimensions. Also, the measured channels are used to validate analytical models. The hardware platform is implemented with a custom-built casing. Finally using a 3D coil, the sensitivity to misalignment is significantly reduced.

# CHAPTER 1 INTRODUCTION

## 1.1 BACKGROUND

Technological advancement in ocean instrumentation is leading to many scientific innovations, including in the field of underwater communications. To communicate to remote instruments, the wireless technology utilized depends on the application requirement, and it is also important to build a reliable communication link for the different underwater environments. Some of the challenges faced in the development of the underwater wireless technology are:

- The cost of deploying and maintaining underwater sensor platforms are extremely high.
- The limited battery life affects the deployment time of the nodes.
- There is a tremendous amount of data (> 1 Terabytes) being recorded on daily basis, which needs to be retrieved and processed frequently.

The above-mentioned needs provide significant interest for commercial, environmental and military applications. While acoustic transmission is the preferred technique for long range applications, magnetic induction is an interesting alternative communication technique for short range applications, particularly because of its immunity to noise, and low-latency. Communication systems relying on magneto-inductive (MI) coupling are commercially available for communication between divers and for remote acquisition of data by Autonomous Underwater Vehicle (AUVs). However, the range is short, and the bitrate remains modest. In this thesis, the objective is to characterize the magneto-inductive

communication link to optimize the link capacity, constrained on the range. For this purpose, theoretical models will be validated using measurement campaigns.

MI is a promising physical layer technique for underwater wireless communication that propagates underwater, since the attenuation rate of magnetic fields doesn't not vary from that of air due to the similar magnetic permeabilities of both medium [1]. In addition, since the magnetic field is generated in the near-field, it is non-propagating and does not have multipath modes. These physical properties of magnetic fields enable communication through shallow, deep and surf zones where noise, reflectivity, delays, multipath propagation weaken the reliability of acoustic communication. Therefore, MI is strongly recommended over short ranges where acoustic noise levels are severe.

Table 1: Environment impacts over different underwater communications [1]

<b>Characteristics</b>	<b>Underwater Communication Technologies</b>			
	<b>Acoustic</b>	<b>Optical</b>	<b>EM</b>	<b>MI</b>
Impact on marine life	Yes	Yes	No	No
Immune to Acoustic noise	No	No	Yes	Yes
Seabed sediments and marine fouling	No	Yes	Yes	Yes
Smooth transition through the air and water interface	No	No	Yes	Yes
Tolerant to turbulence caused by tidal waves or other activities	No	No	Yes	Yes

Environments such as ocean where the water is salty and more conductive the skin effect will be more and affects the communication. Using low frequency will significantly reduce the skin effect but suffers a lot of background noise which also interrupts the communication. Therefore, to minimize the background noise the transmitter front end is tuned to work with extremely narrow bands.

Magnetic fields are directional and require the transmitter and receiver coils to maintain a specific orientation. Keeping the transmitter and receiver coils with the fixed orientation is not possible when deployed in magnetic field. This directional property of MI greatly affects the robustness and increases the localization challenges too. This require the MI nodes to be Omni directional which can be achieved by using three dimensional coils. Designing the three-dimensional coils also has a trade –off between the communication distance, power consumption and complexity of the system which requires an optimal configuration [2].

- Deployment of underwater sensors is required to monitor the health of the planet.
- Hundreds of sensors can be deployed to sense biological, chemical, and physical properties of an ecosystem.
- A tethered network is supported with Autonomous Underwater Vehicles (AUVs).

**Acoustic transmission** is recognized as a preferred solution for underwater communication, particularly at long range. However, because of the slow speed of sound, the latency is large. Also, the bandwidth is limited because of absorption loss. Coherent

acoustic communication systems have been described and are commercially available. However, the time-variance of the channel limits the ability of the receiver to track the phase in mobile conditions. Finally, the underwater environment is subject to interference. Because of this, significant efforts have been made to deploy communication systems relying on alternate technologies.

For a few years now, **optical communications** have received interest [3] [4], and it has been demonstrated that it is possible to achieve a throughput of a few Mbps, for distance as long as 100~meters, albeit in controlled conditions. Important disadvantages of optical communication that have slowed its commercialization, are its high-power consumption, and its sensitivity to turbidity in realistic sea conditions.

Although **electromagnetic (EM)** transmission attenuates significantly in conductive materials, there have been some attempts to use this technology in underwater communication systems. For example, in [5], the authors document the wavelength, propagation speed, and skin depth, as a function of media conductivity, and in [6] the authors predict the capacity as a function of distance for fresh water and sea water. As expected, the high conductivity of seawater  $\sigma$  equal to  $4 \text{ Sm}^{-1}$  significantly reduces the capacity. For example, in [5], an optimal carrier frequency of 30 kHz is chosen so that the 40 cm radius dimensions is a non-negligible fraction of the wavelength, and conductive losses due to eddy currents in seawater remain reasonable.

Table 2: Comparison merits of different underwater communications [1]

<b>Underwater communications</b>	<b>Range</b>	<b>Security</b>	<b>Data rates</b>	<b>Channel disadvantages</b>
<b>Acoustic</b>	~100km	Audible	kbps	Environmental noises, multipath, doppler, salinity, temperature, pressure
<b>Optical</b>	~100m	Visible	Mbps	Line of sight, light scattering, ambient light noise
<b>Magneto-Inductive</b>	~100m	Secure	Kbps-Mbps	Conductivity, multipath
<b>Electro-Magnetic</b>	~10m	Secure	Mbps	Conductivity

As an alternative to EM propagation, magneto-inductive coupling (MIC) has been proposed for underwater communication and relies on magnetic field coupling between electrically small coils. In [7], MIC has been described to enable dense high-speed sensor networks. Also, in [8], the authors consider MI for wireless control of autonomous underwater vehicles. In [1], a model based on transformer coupling theory is developed for a link between two coils with a mutual inductance  $M$ . Also, in [9] the H-field in the near field of a 3D transmitter coil for a MIMO transmitter is reviewed analytically, while its response is confirmed using the COMSOL finite element method simulator in [10]. Also, in [11] a low-power modem prototype has been deployed in a test tank in seawater, and the performance of a coherent communication system is demonstrated for a

1-meter separation. Finally, in [12], an extensive measurement campaign is run for a 3D coil from 10 kHz to 100 MHz

While MIC is expected to provide a short-range link on the order of a few meters, it could be used for data offloading applications, and as a relay link to wireless underwater sensors. For this purpose, in the proposed work, MIC is intended for the deployment of small form-factor nodes. To extend the range of the link, a three-element transmitter with coils oriented perpendicular to each other is designed to reduce the sensitivity to misalignment [13]. In comparison to results presented in [12], the analysis is for low-frequency operation using low-cost standard audio equipment.

## **1.2 THESIS OVERVIEW**

This topic introduces the thesis by providing an overview on the motivation, contributions and objectives

### **Motivation**

Advancement in underwater wireless communication systems has been slow because the different wireless communication technologies are generally very sensitive to the environmental conditions. Acoustic communication, commonly used for underwater application suffers from severe multipath, and low propagation speed. While optical communication has received significant interest recently, it is also subject to the turbidity of the water. Alternatively, magneto-inductive (MI) communication is found to be a promising choice to achieve high-speed transmission applied to a short-range communication underwater link, typically shorter than 100 meters. For short-range, noisy

environments, magnetic coupling can provide a highly reliable, low-latency link. It is also immune to multipath distortion, and provides a covert link, since it does not emit acoustic noise.

## Objectives

By using the proposed architecture, the following research objectives were accomplished,

- Study and demonstrate the performance of magnetic coupling in seawater for wireless energy transfer and short-range wireless communications.
- Design of high – rate wireless energy transfer link to recharge underwater instruments.
- Optimize the operating frequency for the coupling between coils in sea water to enable high speed data transfer at ~100kbps.

## Contributions

Based on the above discussion, the thesis focuses on to design and implementation of a Magneto-inductive link which was characterized using a compact 3-Dimesional transmitter front end. The realistic model of the MI link that includes the effect of coupling loss, conductive loss as well as the atmospheric noise was validated using measurement results in a sea water tank. The MI link channel gain was measured as a function of distance and frequency and the measured channel is used to validate analytical models. Finally using a 3D coil, the sensitivity to misalignment is significantly reduced. This work accomplished has been published [14].

### **1.3 ORGANIZATION OF THE THESIS**

The remainder of the thesis is organized as follows.

**Chapter 2:** Analytical Model of the MI link will be presented

Specifically, the near field coupling will be presented with the equivalent transformer channel model, while the impact of losses on the channel gain in conductive materials will be described. Finally, the channel capacity will be derived for a realistic link model

**Chapter 3:** Measurement campaign will be described

Early prototypes were discussed which lead to the fabrication of a 3-element coil has and interfaced to a test apparatus to validate the MI link model. The transmitter array design is described, and the equivalent receiver model is implemented.

**Chapter 4:** Measured channel gain will be compared to the theoretical channel gain

Deployment of the test apparatus is detailed, and the path loss of the MI link is characterized. The ambient noise taken during the measurements is analyzed then, the path loss using Coil facing the receiver coil is analyzed. Finally, the path loss using the combination of the three coils is shown.

**Chapter 5:** Conclusion and Discussions

In conclusion, the expected capacity of a small-form factor low-power MI communication link is confirmed through measurements. Analytical simulations are used to predict a capacity on the order of  $\sim 1$  kbps for a maximum range of  $\sim 10$  meters and at an operating frequency approximately equal to  $\sim 3$  kHz for a range of few meters.

# CHAPTER 2 MAGNETO INDUCTIVE COMMUNICATION SYSTEM

## 2.1 CONCEPT OF MI SYSTEM

MI communication is realized using tightly wound coils that are loosely coupled. Fundamentally, the magnetic field is produced when a time varying current passes through a conducting wire. When the magnetic lines of force pass through the secondary coil, a voltage is induced. The amount of induced voltage is proportional to the fraction of magnetic flux lines generated by the first coil. The transmitter and receiver coil can be made to resonate at its resonance frequency and the current generated is limited by the load resistance  $R_L$ . The resonance occurs when the transmitter coil has minimum LC series reactance.

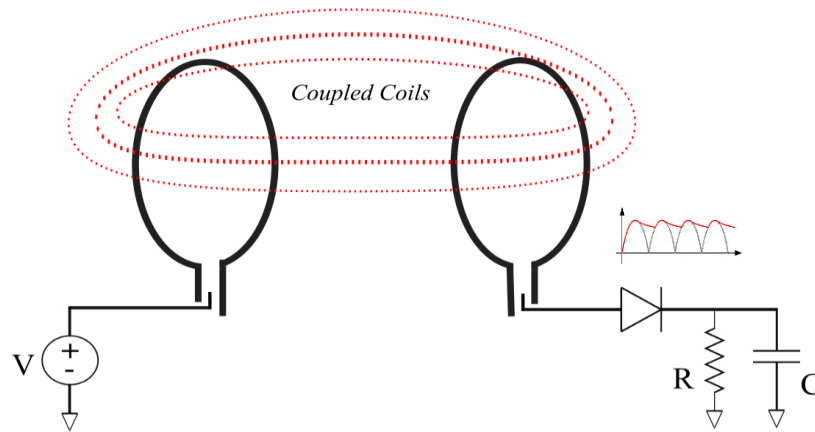


Figure 1: Proposed AC DC Converter

Factors like power, efficiency, size and shape of the coil and the distance between the transmitter and receiver coil greatly affects the voltage induced in the secondary coil. Also, the relative permeability  $\mu$  and conductivity  $\sigma$  of the medium affect the energy received at the receiver. However, conductivity of the medium affects introduces losses due to eddy current for a time varying field. The losses are characterized using the skin depth as will be explained in detail in further chapters.

A simple circular one-dimensional coil exhibits a strong directionality because the magnetic field crossing the receiver plane is stronger when it is perpendicular to the coil surface. Consequently, the induced voltage in the receive coil is higher when the receive coil faces the transmit coil. For this reason, a system with multiple coils is often necessary for MI communication system to achieve short range omni directional communication.

## **2.2 STATE-OF-ART**

In this Section, we discuss previous work related to underwater MI communication, specifically for power and data transfer over a short range with high efficiency. The majority of work on underwater communication has mainly been based on acoustic communication, and we introduce a new underwater communication model called Wireless Magneto-Inductive (MI) power and data transfer.

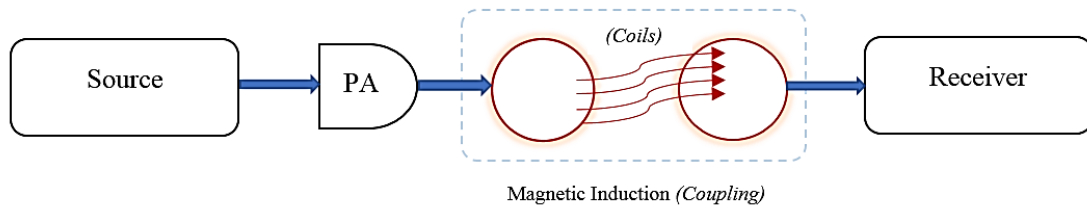


Figure 2 : Schematic block represents MI coupling

The MI based underwater communication exhibits several unique and promising features such as

- Less signal propagation delay
- Constant channel behavior
- Better communication range with high bandwidth
- Stealth underwater operations

The following is a list of comparable work that has been accomplished in the past decade:

**Makoto Ogihara., et.al.** [15] designed a wireless power and data transmission system using a pair of coils and transferred power and signal by using electromagnetic induction. The authors found that the system supports high power transfer (80 % efficiency), high communication quality (BER 0.1 %) and high data rate (40 kbps) by using a single hardware unit. The underwater data communication is modulated by OFDM with center frequency 110 kHz and effective data rate is around 40 kbps using single hardware for both power and data transmission, while the two nodes are kept 30 mm apart.

**Manikandan. J., et.al.** [16] proposed and developed a contactless battery charging mechanism using two approaches. Their power transfer system is capable of charging 28 W, 42 W and 300 W underwater battery-operated systems such as remote operated vehicles (ROVs), autonomous underwater vehicles (AUVs) and wireless sensor nodes under three mediums air, pure water and sea water.

**Neil W. Bergmann., et.al.** [17] demonstrated an underwater wireless sensor network by means of underwater coupling from the sensor hub to the transducer module with a two-way data communication between hub and the transducer. The experiments were carried out with a ZigBee transceiver operating at **2.4 GHz band**, which can communicate with low error rates (**-3 dBm**) up to **70 mm** in sea water and can transmit low power in the **50-100 mW range** with an efficiency of **50%**.

**Marie Domingo., et.al.** [1] developed a model of the MI communication link by representing the near field coupling between two coils. Using a non – ideal transformer equivalent circuit, the mutual inductance is used to extract the attenuation due to the loose coupling between transmitter and receiver. Moreover, the propagation loss is on the high side because of the conductivity of seawater. The performance of the MI system over the path loss was analyzed over the short distance of 9m in both freshwater and seawater with respect to EM and acoustic systems.

## 2.3 MI SYSTEM DESCRIPTION

### 2.3.1 Magnetic Transmission

Magneto- inductive communication systems operate typically over a very short range in the order of few tens to hundreds of meters. A near field magnetic-induction systems is a short range wireless physical layer that communicates by a tight, low power, non-propagating magnetic field between the devices. A transmitter coil in one device modulates a magnetic field which is measured by means of a receiver coil [1]. An underwater communication system that uses MI transmission needs to be modeled carefully taking coupling loss, path loss and conduction losses into consideration. It follows the basic loosely coupled transformer theory into its two – port equivalent network architecture of its dual antenna set up.

As defined by the Biot - Savard law [18], current flowing in a coil will generate a magnetic flux density  $B$  that is perpendicular to the current flow. This phenomenon is shown in Figure 3 ,the flux crossing a surface is a scalar that is derived by integrating the magnetic flux density over the surface that it crosses, such as:

$$\Phi = \int B \cdot ds \quad (2.1)$$

In a transformer,  $\Phi_{12}$  is the flux crossing a secondary coil due to the current flowing in the primary coil, while the total flux crossing the primary coil due to the current in the primary is  $\Phi_1$ . Hence, the total flux due to the current  $I_1$  in the primary is  $\Phi_1 = \Phi_{11} + \Phi_{12}$ , where  $\Phi_{11}$  represents loss due to imperfect coupling. The coupling between the coils is represented using the mutual inductance, which is defined as

$$M = \frac{\Phi_{12}}{i_1}, \quad (2.2)$$

and represents the flux in the secondary per unit current in the primary  $i_1$ . The mutual inductance can serve to evaluate the induced voltage at the secondary  $V_{12}$  due to the current in the primary  $i_1$  such that

$$V_{12} = M \frac{di_1}{dt}. \quad (2.3)$$

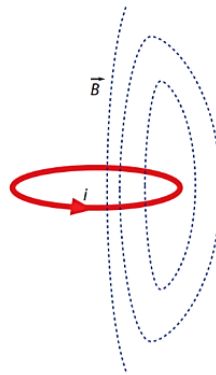


Figure 3: Magnetic flux density representation for current in a coil

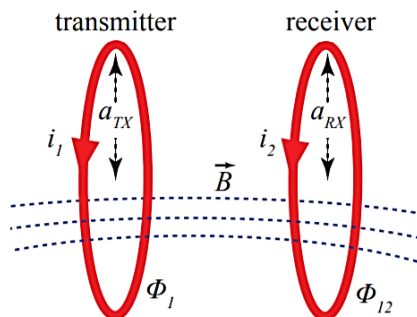


Figure 4 :Magnetic flux  $\Phi_{11}$ ,  $\Phi_{12}$  generated by current  $i_1$

From [19] [20], the magnetic field  $B$  at distance  $r$  from a transmitter coil in a material with permeability  $\mu_0$ , transmit current  $I_{TX}$ , number of turns  $N$  and coil radius  $a$  is

$$B = \frac{\mu_0 I_{TX} N a^2}{(2(a^2 + r^2))^{3/2}}. \quad (2.4)$$

For a given angular frequency  $\omega_{res} = 2\pi f_{res}$ , the voltage induced at a receiver spanning a surface  $S$  with an angle of arrival of the signal  $\alpha$  is,

$$V_{out} = \omega_{res} B N S \cos\alpha \quad (2.5)$$

Note that by adding a capacitance  $C_{RX}$  in parallel with the inductor such that the receiver operated at resonance, the output voltage in the equation (2.5) is multiplied by the loaded quality factor  $Q$  of the tuned circuit, which can be varied from 5 to 50 in typically at low frequency near field applications [19], Hence the receiver can be optimized for higher sensitivity. Effectively, the power gain of the magneto - inductive communication link is equal to

$$G_C = \frac{V_{out}^2}{R_{RX}} \cdot \frac{1}{I_{TX}^2 \cdot R_{TX}} \quad (2.6)$$

The demonstration of (2.6) will be demonstrated in the next section.

### Transformer Channel model

The magneto inductive link model relies on a non-ideal transformer equivalent circuit. The power loss due to the sea water conductivity is also considered to establish the overall link path loss. The communication link between the transmitter and receiver coils includes the

transmitter source  $V_i$ , the transformer lumped equivalent model as well as the source impedance,  $Z_{TX}$  and load impedance,  $Z_L$ . The wireless link coupling gain is defined by the mutual inductance  $M$  between the transmitter and receiver.

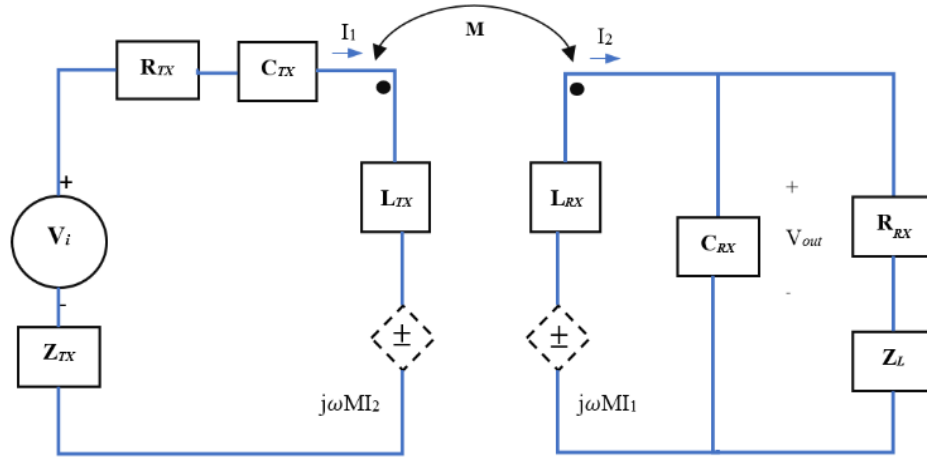


Figure 5: Transformer model MI transceiver

As shown in the Figure 5, the output of the transmitter amplifier is fed to a series resonant circuit. The series resistance  $R_{TX}$  limits the current flowing in to the coil, while the capacitance  $C_{TX}$  is used to ensure that the front-end resonates at the operating frequency. On the receiver end, a parallel capacitance can serve to cancel the self-inductance  $L_{RX}$  at the receiver, and effectively maximize the output voltage  $V_{out}$  measured at  $R_{RX}$ .

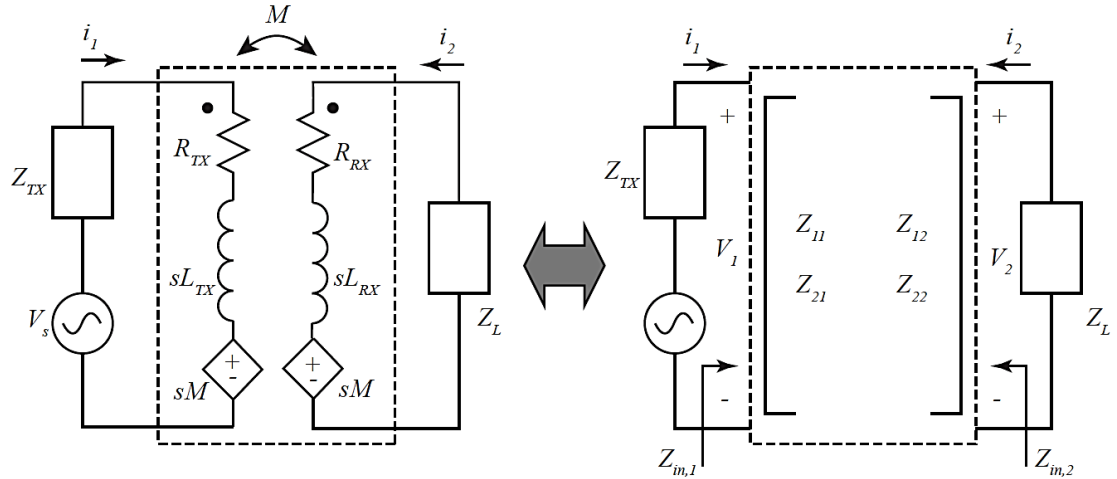


Figure 6 : MI transformer model to equivalent two - port network [11]

Alternatively, the MI link coupling loss is derived analytically using the dual antenna set up which can be easily compared to the two – port network architecture as shown in the Figure 6. Consider that magnetic coupled antennas from the underwater transmitter and underwater receiver are separated by a distance  $r$ .

It is assumed that input voltage  $V_1$ , input current  $I_1$ , output voltage  $V_2$ , and output current  $I_2$  of the dual antenna system are same for the two – port network. It can be described in the matrix form represented by  $z$  – parameters as

$$\begin{pmatrix} V_1 \\ V_2 \end{pmatrix} = \begin{bmatrix} Z_{11} & Z_{12} \\ Z_{21} & Z_{22} \end{bmatrix} \begin{pmatrix} I_1 \\ I_2 \end{pmatrix} \quad (2.7)$$

We can express  $V_2$  as  $V_2 = (I_2) (-Z_L)$  then the equation (2.7) becomes,

$$\begin{pmatrix} V_1 \\ -Z_L I_2 \end{pmatrix} = \begin{bmatrix} Z_{11} & Z_{12} \\ Z_{21} & Z_{22} \end{bmatrix} \begin{pmatrix} I_1 \\ I_2 \end{pmatrix} \quad (2.8)$$

Where  $Z_{11} = R_{11} + jX_{11}$  and  $Z_{22} = R_{22} + jX_{22}$  represents the self-impedances,  $Z_{12}$  and  $Z_{21}$  are the mutual impedances,  $Z_{12} = Z_{21} = jM$  of the two-port system.

## Channel Path Loss

The path loss for the MI communication system by assuming no losses on either side of the antenna coil of the dual antenna system, the transmitted and received powers for a transmission distance  $r$  are given by [1],

$$P_{TX}(r) = \text{Re} (V_I I_I^*) \quad (2.9)$$

Substituting equation (2.9) with  $V_I$  compared with the (2.8) we get,

$$P_{TX}(r) = \text{Re} \left( Z_{11} - \frac{Z_{12}^2}{Z_L + Z_{22}} \right) |I_1|^2 \quad (2.10)$$

$$P_{RX}(r) = |I_2|^2 \text{Re} (Z_L) \quad (2.11)$$

Similarly substituting equation (2.8) in (2.11) we get,

$$P_{RX}(r) = \text{Re} (Z_L) \left( \frac{|Z_{12}|^2}{|Z_L + Z_{22}|^2} \right) |I_1|^2 \quad (2.12)$$

We can observe that both the transmitted and received powers decrease as the distance increases. Note that power in the MI system is not really lost but in fact not transmitted [1]. For comparison of the MI system with the EM and acoustic systems, the transmitted power of the MI system is redefined as,

$$P_{TX}(r_o) = |I_1|^2 \text{Re} (Z_{11}) \quad (2.13)$$

It represents the transmitted power for a very small distance  $r_o$  between the transmitter and receiver. Therefore, the pathloss PL can be defined as,

$$PL = - 10 \log \frac{P_{RX}(r)}{P_{TX}(r_o)} \quad (2.14)$$

$$= -10 \log \frac{R_L(R_{12}^2 + X_{12}^2)}{R_{11}[(R_L + R_{22})^2 + (X_L + X_{22})^2]} \quad (2.15)$$

From the above equation it clearly shows that the received power depends on the load impedance  $Z_L$ . In order to maximize the received power, the load impedance is designed to be equal to the complex conjugate of the input impedance at port 2, which can be expressed as,

$$Z_L = \overline{Z_{input}^{(2)}} \quad (2.16)$$

we can derive  $Z_{input}^{(2)} = \frac{V_2}{I_2}$  from (2.8) when port 1 is terminated by the source impedance  $Z_{TX}$ . Therefore,

$$Z_{input}^{(2)} = Z_{22} - \frac{Z_{12}^2}{Z_{TX} + Z_{11}} \quad (2.17)$$

In an inductively coupled system as shown in the Figure 6,  $L_{TX}$  would be the antenna at the transmitter.  $L_{RX}$  represents the antenna of the receiver,  $R_{TX}$  and  $R_{RX}$  are the coil resistances of the transmitter and receiver antennas. A time varying magnetic flux in the coil  $L_{TX}$  induces a voltage  $V_{out}$  in the coil  $L_{RX}$  due to the mutual inductance  $M$ . From equation (2.5) the mutual impedances ( $Z_{12}$ ,  $Z_{21}$ ) and self-impedances ( $Z_{11}$ ,  $Z_{22}$ ) of the transmitter and receiver antennas are given by,

$$Z_{11} = R_{TX} + j\omega L_{TX} \quad (2.18)$$

$$Z_{22} = R_{RX} + j\omega L_{RX} \quad (2.19)$$

$$Z_{12} = Z_{21} = j\omega M \quad (2.20)$$

where  $\omega = 2\pi f$ , is the angular frequency of the transmitting signal,  $L_{TX}$  and  $L_{RX}$  are the self-inductances and  $M$  represents the mutual inductance. The link gain decreases with the square of the mutual inductance  $M$  between two coils can be calculated as,

$$M = \frac{\pi\mu N_{TX}N_{RX}a_{TX}^2a_{RX}^2}{2\sqrt{(a_{TX}^2+r^2)^3}} \quad (2.21)$$

where  $\mu$  is the magnetic permeability,  $\mu = \mu_o \cdot \mu_r$ , [ $\mu_o$  is the magnetic constant,  $4\pi \times 10^{-7} \text{ Hm}^{-1}$ ,  $\mu_r = 1$  is the relative permeability of water.  $a_{TX}$  and  $a_{RX}$  are the radii of the transmitter and receiver coils, respectively,  $N_{TX}$  and  $N_{RX}$  number of turns in the primary and secondary coils, and  $r$  is the distance between them which is from center of the coils in  $x -$  direction.

The self-inductance  $L$  of a circular loop antenna with  $N$  turns,  $a$  wire radius and a coil radius  $r$  is expressed as,

$$L = N^2\mu r \left[ \ln\left(\frac{8r}{a}\right) - 2 \right] \quad (2.22)$$

The resistance of the conductor increases with frequency due to skin effect, while its dc resistance is expressed as,

$$R_{dc} = 2\rho N \frac{r}{a^2} \quad (2.23)$$

where  $\rho$  is the electrical resistivity with  $N$  number of turns of the coil,  $a$  is the coil radius. However, for frequencies below 1 MHz, the additional resistance is negligible. In fact, for the frequencies of interest, the total parasitic resistance  $R_P$  of the coil is much smaller than

the transmitter resistance  $R_{TX}$ , and hence it can be ignored. The coil is typically a large inductor  $L_{TX}$  that generates the magnetic field in series with a parasitic resistance  $R_P$ . The Q-factor for the inductor is defined as,

$$Q = \frac{\omega L_{TX}}{R_P} \quad (2.24)$$

The Q-factor is typically very large to generate large magnetic field. Hence, if the system operates away from the resonant frequency, a large voltage is required to maintain a constant current. To reduce the required voltage amplitude, a variable capacitance is used to operate at the resonant frequency defined as:

$$\omega = \frac{1}{\sqrt{LC}} \quad (2.25)$$

Because, the MI communication system is wideband, the coil bandwidth is much narrower than the system bandwidth. For this purpose, the capacitor is dynamically tuned to track the instantaneous operating frequency.

The coupling coefficient is the fraction of the total flux emanating from one coil that links the other coil. The mutual inductance cannot be greater than the geometric mean of the self-inductance of the coils ( $M \leq \sqrt{L_1 L_2}$ ). The extent to which the mutual inductance  $M$  approaches the upper limit is specified by the coefficient of coupling  $k$ , where it lies,  $0 \leq k \leq 1$ ,  $0 \leq M \leq \sqrt{L_{TX} L_{RX}}$  and expressed as,

$$M = k\sqrt{L_{TX} L_{RX}} \quad (2.26)$$

MI communication uses well-tuned coils to create an alternating magnetic field. The magnetic field is often bounded within the near field region from the transmit antenna.

If  $\frac{\lambda}{2\pi} \gg d$ , where  $\lambda$  is the signal wavelength, then  $d$  represents the near field boundary away from the transmitter.

Assuming  $Z_{TX} \approx 0$  and using the equations (2.17) (2.18) (2.19) (2.20) in (2.16), the load impedance at the receiver can be derived as,

$$Z_L = R_{RX} + \frac{\omega^2 M^2 R_{TX}}{R_{TX}^2 + \omega^2 L_{TX}^2} + j \left( \frac{\omega^3 M^2 L_{TX}}{R_{TX}^2 + \omega^2 L_{TX}^2} - \omega L_{RX} \right) \quad (2.27)$$

The pathloss for the two-port system can be expressed when equating the values to the equation (2.15) and is given by,

$$PL = -10 \log \left[ \frac{(\omega_{res} \cdot M)^2 \cdot R_L}{R_{TX} (R_L + R_{RX})^2 + R_{TX} (X_L + \omega_{res} L_{RX})^2} \right] \quad (2.28)$$

Similarly using (2.21) (2.22) (2.23) (2.27) in (2.28) the path loss for MI is obtained.

$$PL_{MU} = -10 \log \left[ \frac{(\omega_{res} \cdot M)^2 \cdot R_L}{R_{TX} (R_L + R_{RX})^2} \right] \quad (2.29)$$

where  $\omega_{res}$  is the angular resonant frequency  $\omega_{res} = 2\pi f_{res}$ . As can be seen from (2.29) equation [11], the received power is increased by reducing  $R_{TX}$ . As expected power decreases with a decrease of the mutual inductance  $M$  squared.

Note that the path loss  $PL_{MU}$  derived represents the power deliver to the load, with respect to the power delivered to the input of the network. To maximize the power transfer, the transmitter source impedance which is equivalent of the power amplifier output impedance should be equal to the impedance of the transmit coil.

### 2.3.3 Loss in Seawater

Additionally, to the coupling loss in a conductive material, such as sea water, the magnetic field generates undesired eddy currents, which produce ohmic losses in the medium. The eddy currents generated by the ac magnetic field flow in salt water and waste energy, since they produce a negative moment that bucks the transmitted moment and also modifies the field distribution. The main parameter to measure eddy currents is the skin depth [21] . Attenuation is the inverse of skin depth  $\alpha = \frac{1}{\delta}$ , which is given by,

$$\alpha = \sqrt{\pi f \mu \sigma} \quad (2.30)$$

where  $\sigma$  is the electrical conductivity of the sea water is approximately equal to  $5 \text{ Sm}^{-1}$  at  $f = 1\text{kHz}$  the skin depth is approximately 7 meters. The skin depth can be used to calculate the conductive loss at varying distances with in a conductive material. Therefore, the power gain in a conductive material is given by,

$$PL_{\alpha} = -20 \log(e^{\frac{r}{\delta}}) = 8.69 \alpha r \quad (2.31)$$

Effectively, the total magneto – inductive link loss becomes,

$$PL_{MU} = PL_{\alpha} + G_C \quad (2.32)$$

$$PL_{MU} = -20 \log(e^{\frac{r}{\delta}}) + \frac{V_{out}^2}{R_{RX}} \left( \frac{1}{I_{TX}^2 \cdot R_{TX}} \right) \quad (2.33)$$

As result, the total path loss in sea water,  $PL_{sea}$  is given as [1],

$$PL_{sea} = PL_{MU} + PL_{\alpha} \quad (2.34)$$

$$PL_{sea} = -10 \log \frac{(\omega_{res} \cdot M)^2 \cdot R_L}{R_{TX} (R_L + R_{RX})^2 + R_{TX} (X_L + \omega L_{RX})^2} - 20 \log(e^{\frac{r}{\delta}}) \quad (2.35)$$

As discussed earlier the total path loss increases with distance  $r$ , at low frequency, the conduction loss is negligible and total loss is equal to the coupling loss. However, the coupling loss is smaller at high frequency. This indicates that an optimal frequency should be chosen to maximize range, as will be discussed in further chapters.

## **2.4 FREQUENCY DEPENDENT NOISE:**

Signal transmission through any communication channel suffers from additive noise, which is generated internally by the active or passive components such as resistors and solid-state devices used to build the communication system and is termed as Thermal Noise. These noises can also be generated externally because of interference from other channels. Noise is one of the main limiting factors in a communication system because when noise is added to the signal, it is highly complicated to transmit information over a finite bandwidth communication system.

### **Thermal Noise:**

Thermal noise or Nyquist noise is often generated due to the thermal agitation of electrons inside the volume of conductors or resistors even in the absence of electric field. If the noise at the receiver is purely thermal, its normalized noise power spectral density (PSD) is given by,

$$N(f) = 4kT_o \quad (2.31)$$

where  $k = 1.38 \times 10^{-23} \text{ JK}^{-1}$  is the Boltzmann's constant and  $T_o$  is the receiver temperature in Kelvin [22].

## Atmospheric Noise

Atmospheric noise is a collective term of all noise sources that are not local thermal. A typical example of atmospheric noise is receiver noise. It may be caused by the electrical activity in the atmosphere as well as by man-made electrical disturbances. In lower frequency ranges, ambient noise is picked up by the antenna, especially if the antenna is at the surface and dominates over thermal noise. Therefore, it is preferable to use a noise model that is analogous to the thermal noise.

According to [8], a basic model for the magnetic field penetration consists of a cubic distance  $r^3$  attenuation combined with the absorption loss is given as,

$$|B(f, r)| = \frac{\alpha(T)}{4\pi r^3} \quad (2.36)$$

The attenuation  $\alpha(T)$  represents the exponential medium loss with respect to skin depth and its frequency dependent, since skin depth  $\delta$  is frequency dependent and has low pass characteristics and is given by,

$$\alpha(T) = 2e^{-T_o} \sqrt{T_o^2 + (1 + T_o^2)} \quad (2.37)$$

In the following, we define the atmospheric noise power density as

$$N(f) = \frac{4kT_o F_a(f) R_r}{R} \quad (2.38)$$

where  $R_r$  is the radiation resistance of the antenna,  $R$  is the ohmic resistance of the receiver coil, and  $F$  is the atmospheric noise temperature given by

$$F_a(f) = \frac{6\pi Z_0 B^2}{k_0^2 4kT_0} \quad (2.39)$$

where  $k_0$  is the wave number and is equal to  $k_0 = \frac{2\pi f}{c}$  (where  $c$  is the speed of light) and  $Z_0$  is the impedance of free space.  $Z_0$  also equals the ratio of the electric field component to the magnetic field component  $Z_0 = \frac{|E|}{|B|}$  and is approximately  $377 \Omega$ . To deliver the atmospheric noise as a function of frequency and atmospheric noise temperature in the following

$$F_k = \sqrt{F_a \frac{k_0^4 Z_0}{6\pi}} \quad (2.40)$$

Equating the values and applying logarithmic on the above equation,

$$20 \log F_k = 10 \log F_a + 40 \log f - 294.147 \quad (2.41)$$

Using MI, it is recognized that atmospheric noise produces significant interference at low frequency. According to [20], the atmospheric noise temperature ratio  $F_a$  reaches several hundred dBs below 10 kHz. In this work, the contribution of the thermal noise voltage  $\sqrt{4kT_0 B R_{LD}}$  in the load resistance  $R_{LD}$  is added to the atmospheric noise  $\sqrt{4kT_0 B F_a R_r}$  in the radiation resistance  $R_r$  to assess the MI link capacity. Note that  $k$  is the Boltzmann's constant and  $T_0$  is the ambient noise temperature. Also, the radiation resistance  $R_r$  of an electrically small loop antenna can be found in [22].

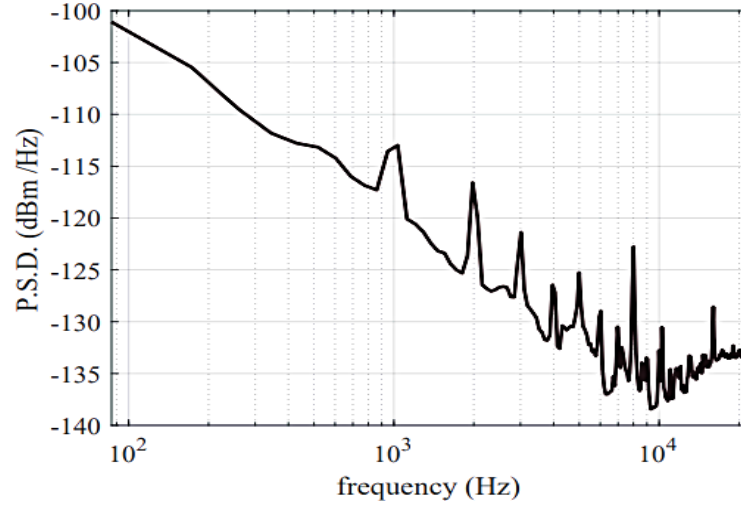


Figure 7: Measured atmospheric noise

## 2.5 OPTIMUM FREQUENCY SELECTION

According to [11], the effect of the carrier frequency on the bandwidth and communication distance is shown in Figure 8, for different number of turns. Note that the transmit front-end capacitance is adjusted to maintain resonance as the frequency is swept. For a fixed number of coils, the bandwidth is constant above a specific frequency. This is expected since, for a high-quality factor, the bandwidth  $B$  of the coil is,

$$B = \frac{f_{res}}{Q} \quad (2.42)$$

$$\text{Also, } B = \frac{R_{RX}}{2\pi L_{TX}} \quad (2.43)$$

In other words, the bandwidth is frequency independent for a fixed inductance. A corner frequency is observed on the system bandwidth in Figure 8, below this frequency the bandwidth is limited by the condition to fix the bandwidth to 20% of the carrier frequency.

To maximize the communication distance, an optimum frequency exists as shown in Figure 8. Below the optimum frequency the total path loss is dominated by coupling loss since the wavelength is much greater than the coil dimensions, whereas above the optimum frequency, loss due to conductivity in sea water dominates. Note that below a frequency slightly higher than the optimum frequency, the communication link operates in the narrowband limited condition: the transmit signal bandwidth is limited to be 20% of the carrier frequency. Effectively, to maintain a high throughput, it is preferable to operate at a frequency above the optimum frequency.

For example, for a coil design with 24 turns, the optimum frequency to maximize range is approximately 10 kHz. However, for a center frequency of 23 kHz, the bandwidth is increased to 3600 Hz for a marginal decrease in range down to 4.7 meters instead of 5 meters. To provide an additional degree of freedom, the number of turns can be varied. As observed, increasing the number of turns can increase the range, but reduces the bandwidth. One can also observe that the corner frequency at which the system becomes narrowband is higher when the number of coils is reduced. For example, with 120 turns on the loops, the maximum distance is 12.9 meters at a frequency of 1 kHz. However, its bandwidth is limited to only 143 Hz.

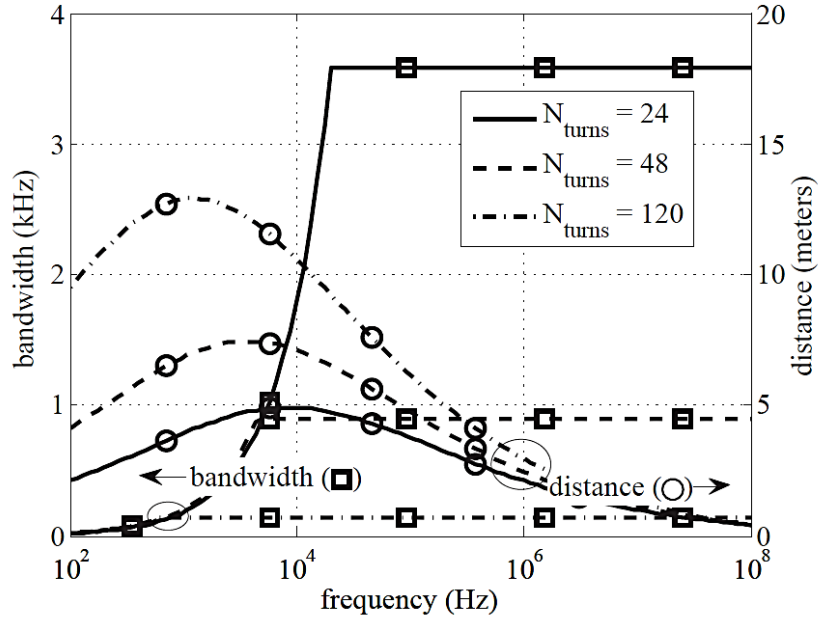


Figure 8: Communication bandwidth (identified by squares) and distance (identified by circles) vs. carrier frequency for different number of turns.

To assess the capacity, a relevant range of carrier frequency  $f_c$ , and distances  $r$  between the core and the farthest relay is defined. Using the magneto-inductive link path loss including the coupling loss defined by (2.3), and the conductive loss defined by (2.26) the total path loss  $PL_{tot}$  is evaluated and, for the given transmit power. As such, the received signal power  $P_{RX}$  as a function of  $r$  and  $f_c$  can be obtained through simulation. To estimate the signal-to-noise ratio (SNR) at the receiver, the noise power in a standard  $50 \Omega$  load at the output of the receiver coil includes contributions from the thermal and atmospheric sources, as documented in [20].

The Shannon capacity formula according to [8] is given by

$$C_{wg} = W \log_2(1 + \text{SNR}) \quad (2.44)$$

Where  $W$  is bandwidth in hertz, and SNR is the signal to noise ratio. The Shannon capacity discusses on the fundamental limits on the rate at which we could transmit over the wireless channels. It sets an upper boundary on how fast we can transmit information over a chosen wireless link.

As seen from (2.44) the capacity is directly proportional to the bandwidth and if we have wider bandwidth to communicate, we have high possibility to send more data which affects the MI link modelling as it focuses on narrow band selection.

Shannon's capacity for the MI link can be assessed with the signal to noise ratio of the transit power using,

$$C_{MI} = W \cdot \log_2 \left( 1 + \frac{P_{RX}}{N_o B} \right) \quad (2.45)$$

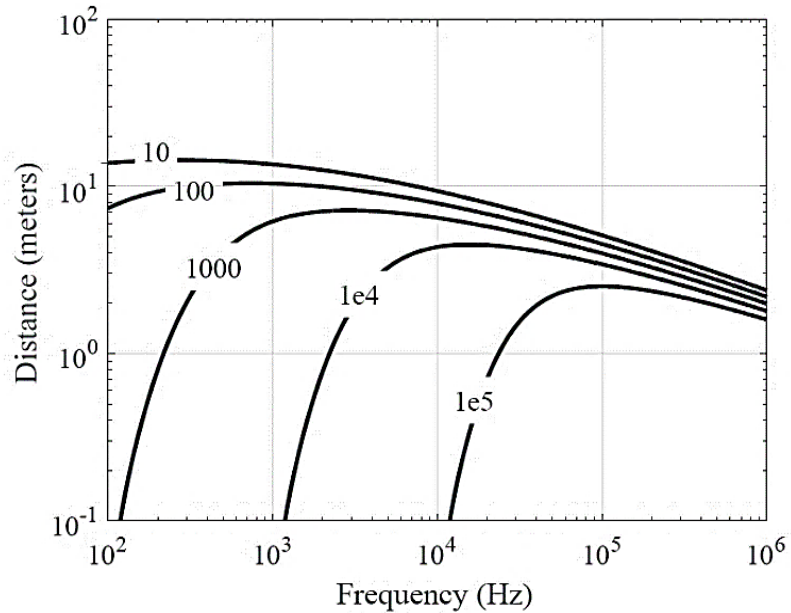


Figure 9: Capacity contour plot as a function of Frequency with Distance

Analyzing the simulation results, the capacity of the magneto-inductive communication link is shown Figure 9, as a function of frequency and distance. Using Figure 9, an optimal carrier frequency  $f_{MI}$  can be chosen to meet the throughput requirements constrained on the hardware. It can be observed that only a very small throughput on the order of 100 bps can be achieved for a range above 10 meters. In contrast, to achieve a 100 kbps for a range of 3 meters, a center frequency close to 100 kHz should be chosen for the MI link. In the next section, a prototype will serve to confirm the MI link model.

## CHAPTER 3 MULTI-COIL IMPLEMENTATION

### 3.1 EARLY PROTOTYPES

#### 3.1.1 Single Coil Setup

An MI communication link is developed and tested using a pair of coils at the transmitter and receiver and the analytical model is confirmed in the near field propagation between the coils. As such, the MI channel loss is measured.

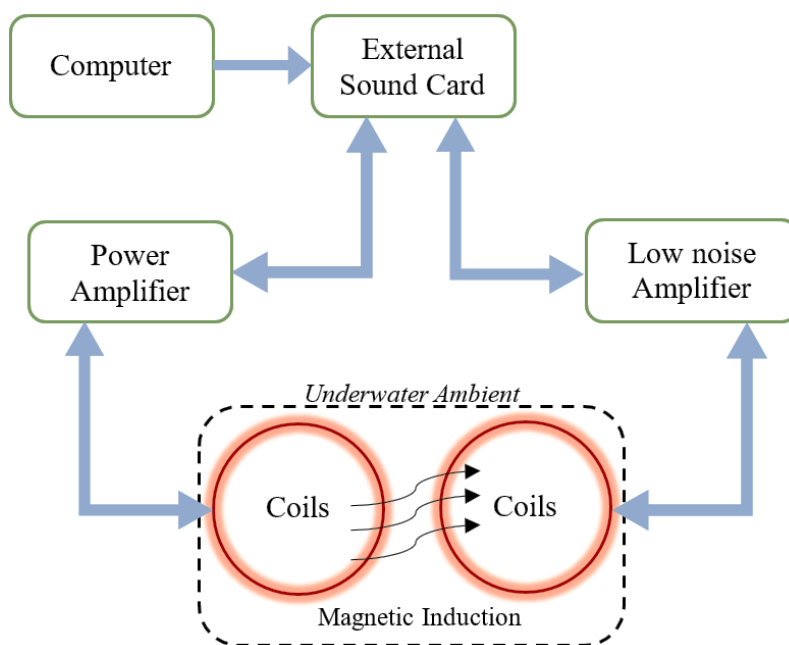


Figure 10: Single coil architecture of initial MI system

The transmit signal was generated using a laptop computer and was amplified by the power amplifier. Then, through the magnetic induction between two identical coils, the signal was

received at the receiver. At the receiver, the signal was amplified and recorded into the computer as an audio file. The complete hardware components list is shown below.

Table 3: Components lists used to implement MI single coil transceiver set up

<b>Components</b>	<b>Description</b>
Power Amplifier	MAX 98400A Evaluation Kit
MI Circular Coils	Two identical coils with 28 turns and 10 cm diameter
LNA	Customized circuit gain of approx. 100
Measurement equipment	Multimeter, Oscilloscope
Aquarium Tank	Square one, with fresh water filled
Accessories	Laptops with external sound cards, load resistors, cables

Table 3 shows the list of components used to build the transceiver, with identical coils composed of 28 turns each and the MAX98400A the EV kit operates from an 8V to 28V DC power supply. The EV kit accepts a pair of single-ended or differential input signals and provides two sets of differential outputs for speakers.

To allow a transmission range on the order of a meter, the antenna radius is set to  $a_{TX} = a_{RX} = 0.25$  m. In sea water, where the conductivity is approximately  $\sigma = 5$ , the skin depth  $\delta$  is 0.22 m and defines the boundary of the near field. The receiver load impedance is equal to  $R_L = 50 \Omega$ . For 20 turns on each coil, and a wire diameter equal too 1 mm, the coil antenna inductance  $L_{TX}$ ,  $L_{RX} = 0.7$ mH and coil resistance  $R_{TX}$ ,  $R_{RX} = 0.6 \Omega$  respectively.

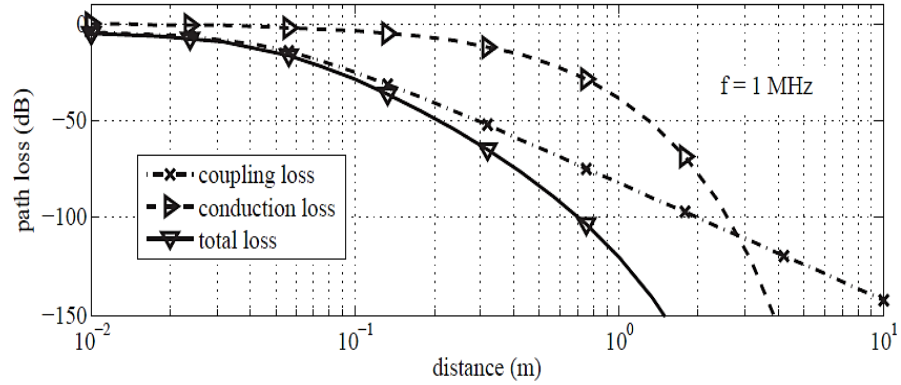


Figure 11: Path loss vs distance at 1 MHz

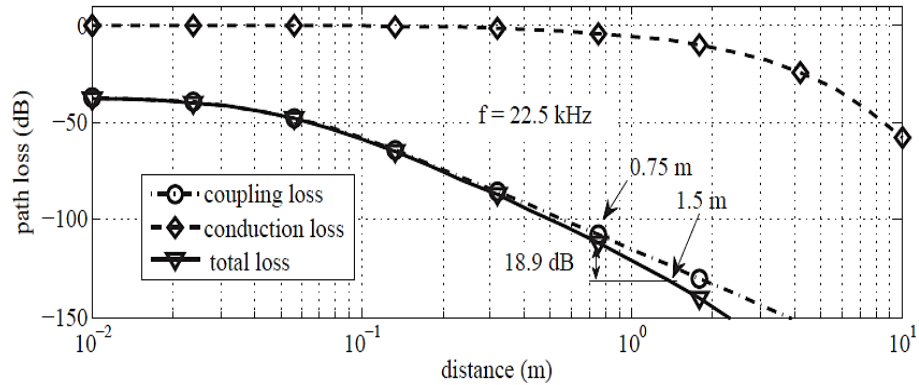


Figure 12: Path loss vs distance at 22.5 kHz

It has been analyzed that to increase the transmit power, the coil loaded Q-factor must be high, thus restricting the bandwidth of the system. To extend the bandwidth, we can dynamically tune the resonant frequency by adjusting the series capacitance  $C_s$  in the transmitter end [11]. Next, a QPSK modulated signal is transmitted from a laptop sound card and amplified using class D power amplifier which provides 18V pulse width modulated signal to a second order filter and its cutoff frequency is approximately 25 kHz.

For the proposed system characteristics, the propagation loss is shown in the Figure 11, Figure 12. As can be observed, for a distance below 20 cm the total attenuation is less than -6 dB but increases very rapidly and at a distance of 2.5 m, the signal has attenuated by 70 dB.

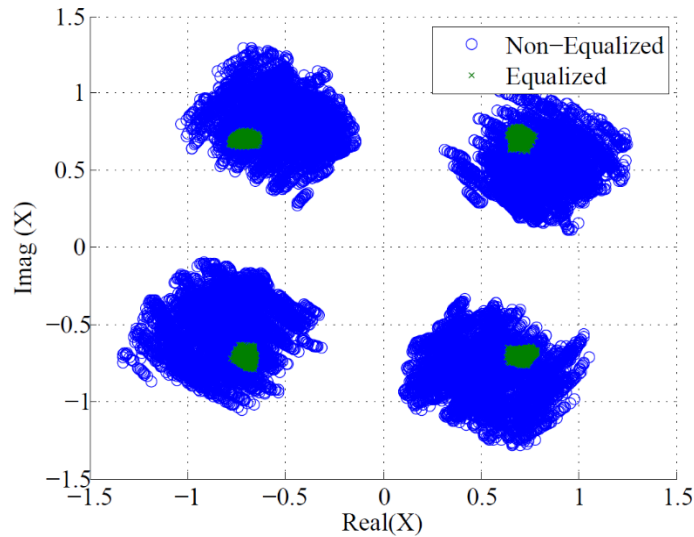


Figure 13: Graph shows the scatter plot of received and equalized signal [11]

The error vector magnitude (EVM) of the signal is extracted before and after equalization. As shown in Figure 13 , before equalization the EVM was -10 dB, while after equalization it was -31.4 dB, for an equivalent SNR equal to 31.4 dB. Using this information for a 0.75-meter deployment, it is possible to extrapolate the SNR at varying distances. For example, using the analytic model of the MI link represented in Figure 11, Figure 12 , the SNR will reach 12.5 dB for a communication range of 1.5 meters, at the edge of the nearfield. The Figure 14 and Figure 15 shown below were the testing prototypes, analyzed as in the

reference [11]. Tests were conducted for both of these prototypes, in air as well as in the aquarium tank filled with water.

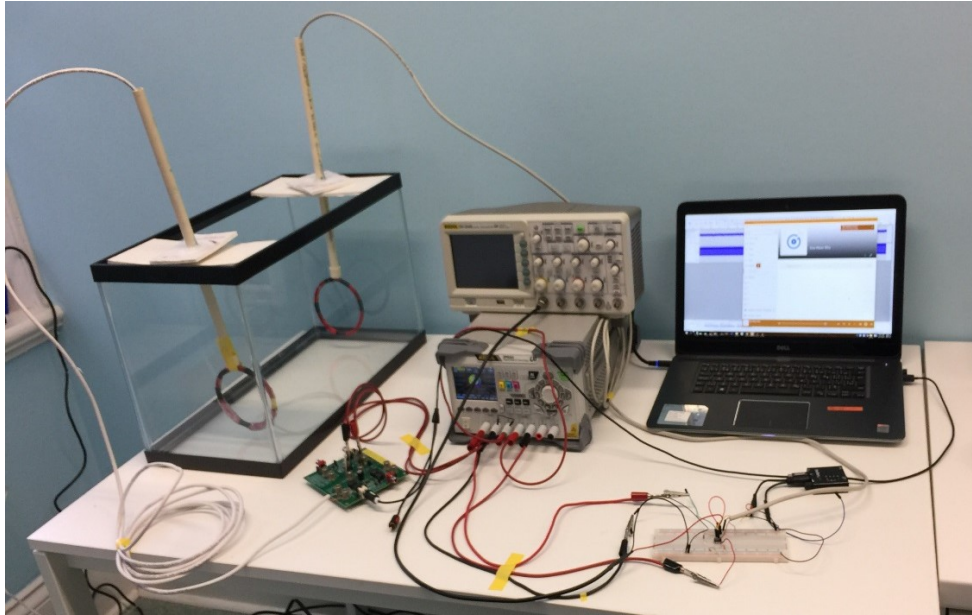


Figure 14: Prototype testing phase

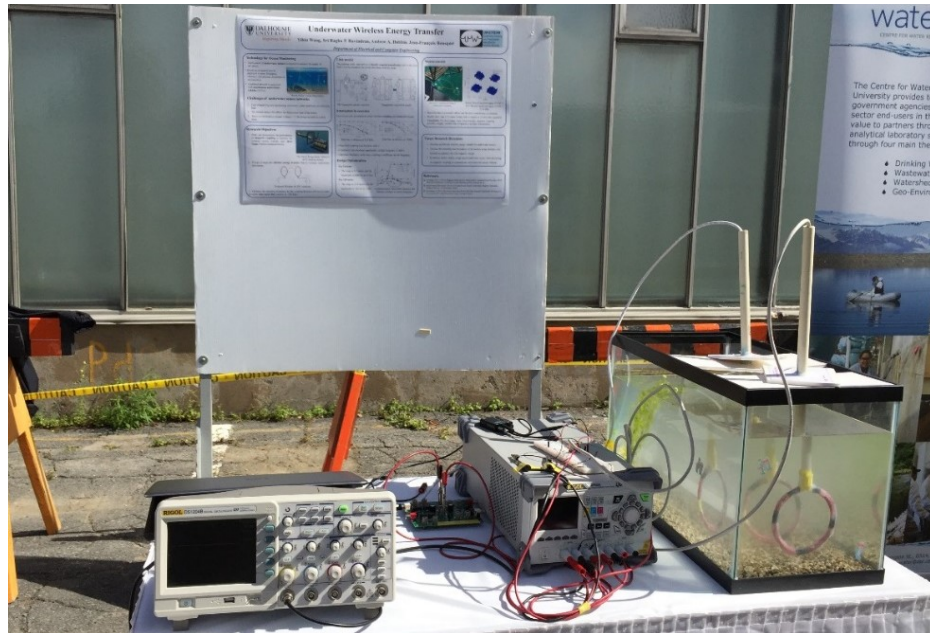


Figure 15: Prototype display at Dalhousie's event

### 3.1.2 Digital Modem interface

In this architecture, we designed and generated signal from the microcontroller in the form of square pulses 2.5V at a frequency in the range few KHz (80 kHz and 120 kHz signal) is sent to the power amplifier with a desirable gain and fed to the output stage Class B amplifier to achieve high efficiency and reduce further DC components before the transmission. The signal is then transmitted between two identical MI coils, and the signal is received at receiver side. The receiver side is designed for high gain to amplify the low received signal due to some loss.

For reference, the implementation Atmel code and picture of the digital modem implemented on a bread board with microcontroller and coils connected is provided in the Appendix E section. The frequency spectrum of an FSK signal is difficult to obtain, this is a general characteristic of FM signals. Consider the case where the binary message consists of an alternating sequence of zeros and ones. If the two frequencies are each multiples of  $1/T$  ( $f_1 = m/T$  and  $f_2 = n/T$ ) and are synchronized in phase, then the FSK wave is a periodic function which is shown in the Figure 16,

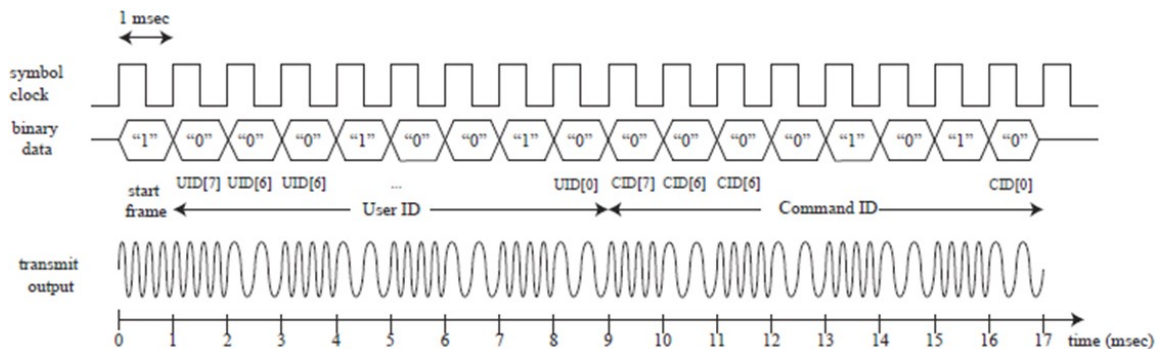


Figure 16: FSK signal shows two frequency of transmission

The frame consists of multiple bits each with a duration of 1 ms. Each period contains many periods of the carrier frequency. When the frequency is 90 kHz, the ATmega 644 embedded processor will record it as a “bit 0”. On the contrary, if the peaks appear in 120 kHz during this bit period, the micro controller will record the data as “1”. Note that the modulated signal output from the micro-controller is a square wave and the peak to peak voltage value is 5 Volts.

First of all, the signal from the digital transmitter will pass through a capacitor, which acts as a high pass filter, to remove the direct current component in this signal. Further the voltage amplification happens in the voltage amplification and output stage amplifier stages. The ac signal after amplification is transmitted and received using the MI coils designed as shown in Figure 17 . The receiver is designed at its high gain setting to retrieve the signal and later it can be rectified and regulated.

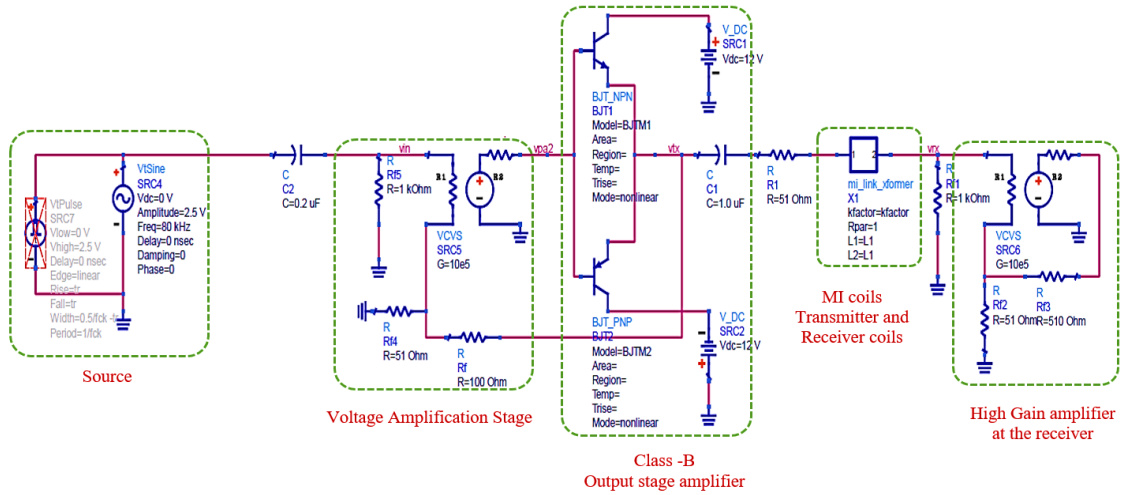


Figure 17: Circuit schematic of a digital Transceiver set up using ADS tool

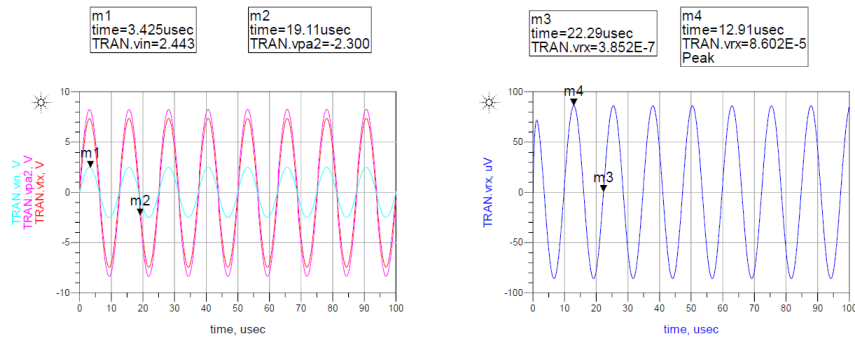


Figure 18: Sinusoidal input of 80Khz frequency, 2.5V<sub>pp</sub>

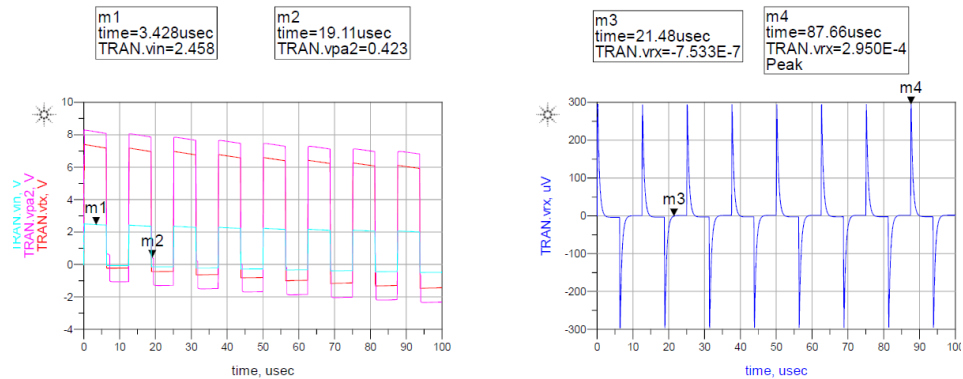


Figure 19: Square input of 80Khz frequency, 2.5V<sub>high</sub> (no sweep)

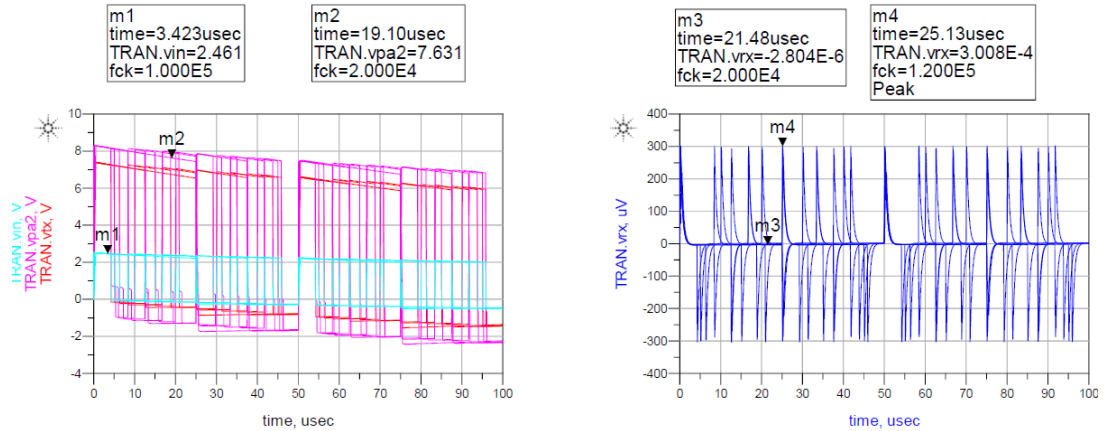


Figure 20: Square input of 80 KHz frequency,  $2.5V_{high}$  (with parametric sweep)

The above Figure 18, Figure 19, shows the simulated output from a sinusoidal input and square wave input with their corresponding frequency sweep. The frequency of 80 kHz at  $2.5V_{high}$  selected as ideal for the system and Figure 20 shows the parametric sweep up to 100 micro seconds for the square wave input.

### 3.2 TRANSMITTER FRONT-END DESIGN

Magneto-Inductive coupling is expected to provide a short-range link on the order of a few meters, it could be used for data offloading applications, and as a relay link to wireless underwater sensors. For this purpose, in the proposed work, MI coupling is intended for the deployment of small form-factor nodes. To extend the range of the link, a three-element transmitter with coils oriented perpendicular to each other is designed to reduce the sensitivity to misalignment [23]. In comparison to results presented in [12], the analysis is for low frequency operation using low-cost standard audio equipment.

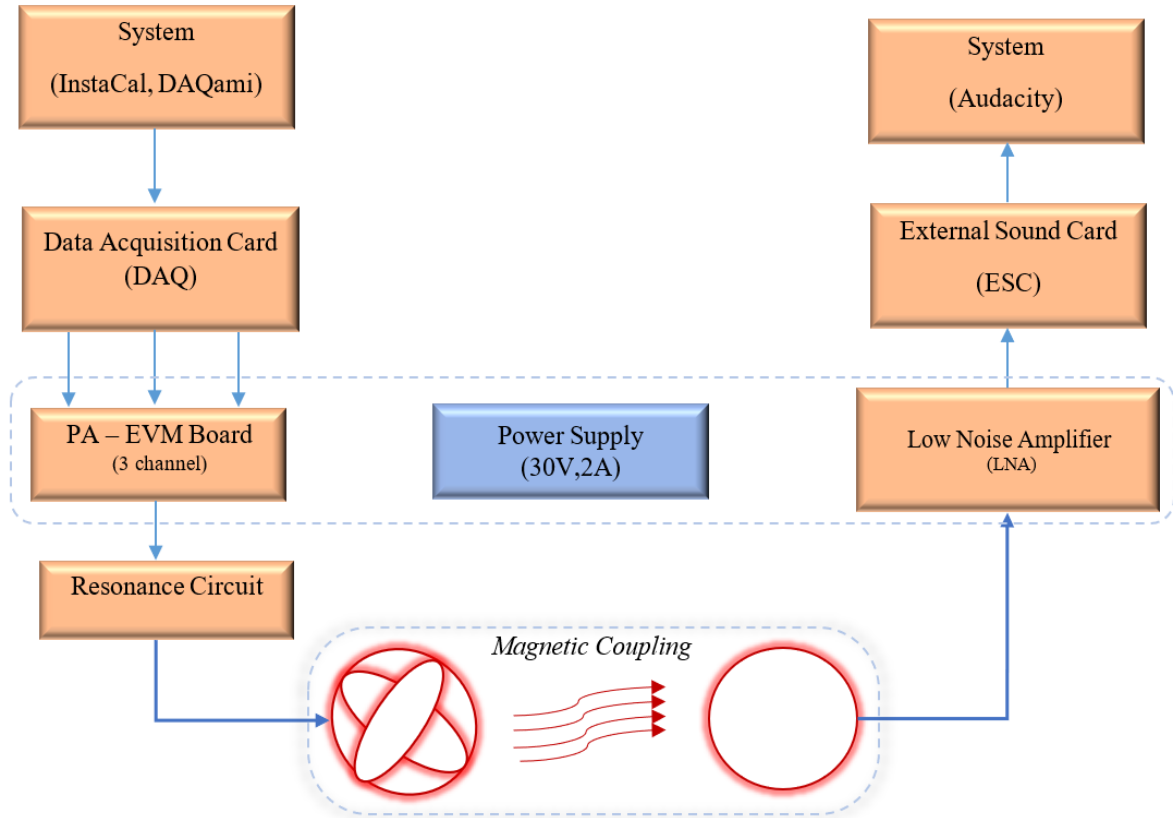


Figure 21: Block representation of implemented multi-coil setup

The front-end specifications are provided to enable a small low-power device that can be deployed for an extended period. At the core, it is expected that the power available at the output of the power amplifier is  $P_{TX} = 0.1W$  and is delivered to the coil in series with a resistance of  $4 \Omega$ . The radius of the coil  $a_{TX}$  is 6.25cm at the core, and to assess the capacity, its number of turns  $N_{TX}$  is adjusted to maintain a quality factor of the transmit front-end equal to  $Q_{TX}$  is 5, such that the bandwidth remains at 20% of the resonant frequency. The geometry of the receiver coil is fixed, such that its radius  $a_{RX}$  is 6.25cm and its number of turns  $N_{RX}$  is 26.

The tones are transmitted at different frequencies ranging from 250 Hz to 10 kHz. These tones were generated using Measurement Computing's DAQ device USB – 3101FS data acquisition card. The software InstaCal - DAQami on this DAQ device gives flexibility up to 10 kHz, simultaneously to work with three channels at the same time or separately with sampling frequency up to 44.1 kHz.

An Audio/Power amplifier is an amplifier which produces amplification of power between the input and output. Power amplifiers play an important role in the transmitter end which required to boost the signal to overcome the transmission channel losses between the transmitter and receiver. PA's are the prime consumers of the power in a transmitter hence while designing a PA we need to know how efficiently DC power can be converted into AC/RF power. Other important aspect of PA design is to preserve the input and output power relationship to maintain the signal integrity which requires the tradeoff between linearity and efficiency.

The power amplifier TAS5630 is a high-performance, integrated Stereo Feedback Analog-Input Digital Amplifier Power Stage designed to drive 4  $\Omega$  speakers at up to 300 W per channel. This amplifier requires only a simple passive demodulation filter to deliver high-quality, high-efficiency audio amplification. This EVM board is configured with 2 BTL channels and the possibility to apply either a single ended or a differential analog input signal. This EVM is a complete stereo analog input 2  $\times$  300 W power amplifier ready for evaluation.

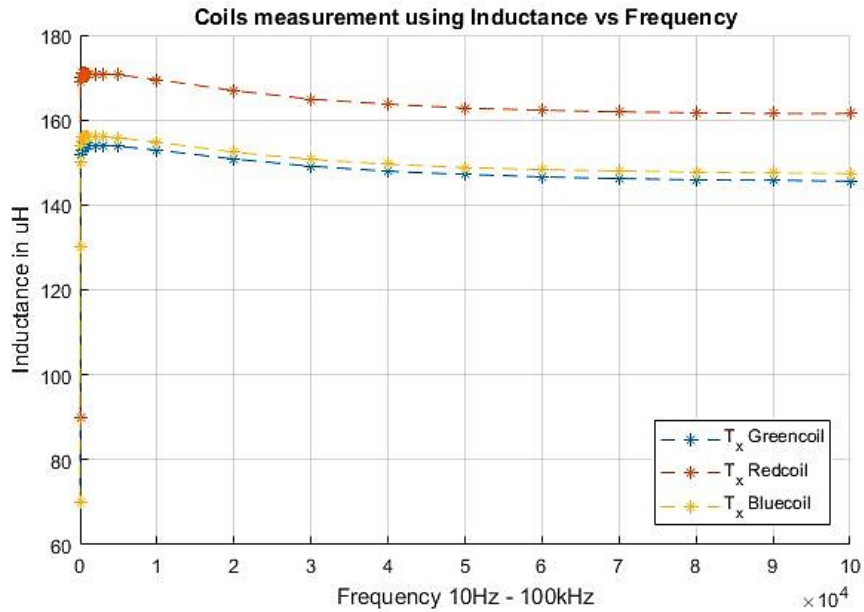


Figure 22 : Inductance plot for multi-coil transmitter

The inductance and quality factor of each transmitter coil is measured and analyzed using the impedance analyzer and the Figure 22 shows that the value of  $L_{TX}$  remains steady over the frequency from 500 Hz to 10 kHz which is taken as the test range of this experiment.

### 3.3 ENCASING THE 3D COIL

The hardware setup used in this experiment needs a careful preparation on sealing various components from the sea water exposure. As the transmitter and receiver will be put to test for a longer period of time, both the transmitter and receiver coils need perfect sealing as the sea water is conductive and corrosive. For the transmitter coils assembly, the three coils

(AWG 18) were wound in circular loop with each coil is perpendicular to one another. The buoy enclosure was constructed using the tool SOLIDWORKS and 3D printed as top and bottom hemispheres as shown in Figure 23.



Figure 23: 3-element coil windings and 3D printed casing

Once the Casing is fitted with the coil , main connection lead were soldered with the 6 - Subconn connector cable and each coil 1,2,3 were marked as red, blue and green corresponding to each of 3-channels. Appendix B gives a brief understanding on the color scheme used. Figure 24 shows the corresponding coil orientation with respect to channel and  $xyz$  axis. The coils were placed inside the top assembly unit and ziptied to minimize the internal movements.



Figure 24: Coil color and channel orientation

As shown in Figure 25, the epoxy is applied in various layer before and after sealing. to enhance the propoer seal between the top and bottom assembly a thin air tight gasket is custom made and bolted the assembly. Last layer of epoxy is coated with the connector cable facing up. Weights were added to support the transmitter perpendicular to the ground during deployment as shown in Figure 29. Also, from Figure 26 we can see that Receiver coil is sealed by gluing the entire coil multiple times and attaching a air tight pipe to it.



Figure 25: Adding connector cables and sealing with epoxy

### 3.4 MAGNETO INDUCTIVE RECEIVER:

The receiver in the MI communication system usually consists of the secondary loop antenna that is receiver Coil  $L_{RX}$ , which is considered to be magnetically coupled with the transmitter loop coil,  $L_{TX}$ .



Figure 26: Sealed receiver coil facing enclosed transmitter

As mentioned in the reference, [20] the induced voltage in the receiver coil via faraday's law due to the AC magnetic flux density produced by a magnetic dipole source as a function of frequency, distance and material parameters is given by,

$$U_f = \omega \mu B \phi_r \quad (3.46)$$

where B is the magnetic field component at the receiver loop and  $\phi_r$  is the receiver antenna merit factor. The induced voltage also depends on the magnetic permeability  $\mu = \mu_0 \mu_r$ , magnetic permeability of free space is given by [ $\mu_0 = 4\pi \times 10^{-7} \text{ Hm}^{-1}$ ], and  $\mu_r = 1$  because most of the materials are non-ferromagnetic.

The magnetic field is attenuated according to the skin depth and in a good conductor with ( $\frac{\sigma}{\epsilon\omega} \gg 1$ ), and if the communication range is within the near field region ( $T \ll 1, r \ll \delta$ ) where T is the ratio of operating distance to skin depth, given as  $T = \frac{r}{\delta}$ . The optimal frequency for a given distance  $r$  is given by,

$$f = \frac{T^2}{\pi \mu r^2 \sigma} \quad (3.47)$$

by using above equations, we can find the induced voltage in the receiver coil. As the frequency goes to zero, the skin depth  $\delta$  becomes large and  $T \rightarrow 0$  so the induced voltage tends to zero and it happened due to the lack of magnetic induction at frequency zero. Similarly, at high frequency the skin depth  $\delta$  becomes small and  $T \rightarrow \infty$ , therefore  $e^{-T} \rightarrow 0$ . As a result, there is no signal because of the greater degree in the skin depth attenuation.

## Receiver Implementation:

The receiver consists of a single coil differentially interfaced to an LT1167 Low-Noise Amplifier (LNA) with  $100\text{ M}\Omega$  input resistance. For the LNA, two gain settings are defined to maintain linearity at short-range and reduce effect of noise at long-range. The output of the amplifier is applied to a sound card and recorded using Audacity for offline processing.

LT1167 is a low power, instrumentation amplifier which requires only one external resistor to vary the gain from 1 to 10,000. The supply ranges from 0.9mA typical for  $\pm 2.3\text{V}$  to  $\pm 15$ . Receiver LNA gain can be estimated using the equation below,

$$\text{Gain} = 1 + \frac{49.4\text{k}\Omega}{R_G} \quad (3.48)$$

When the gear is fully submerged, the link power gain expressed in equation (2.32) can be measured between the transmitter and receiver. For this purpose, the receiver front-end gain between the input of the LNA and the output of the sound file must be a priori characterized.

During the experiments, the receiver coil is normal to the  $y$ -axis shown in Figure 24, and its height is carefully fixed to receive the maximum flux from the transmitter. During the first experiments, transmitter *Coil 1* is facing the receiver coil, and is expected to contribute most significantly to the flux at the receiver. Whereas, *Coil 2* is placed perpendicular to *Coil 1* and not anticipating much flux during signal transmission. The final experiment consists in evaluating the MI link gain as a function of angle in the  $xy$ -plane. In this

orientation, it is expected that the two coils oriented vertically will both contribute with different ratios to the flux at the receiver, while *Coil 3* will have negligible impact.

## CHAPTER 4 MEASUREMENTS

### 4.1 TEST TANK TRIAL

The specific contributions of this work are the characterization of the MIC link using a prototype deployed in a sea tank. The gain of the channel will be compared to the gain predicted by analytical models.

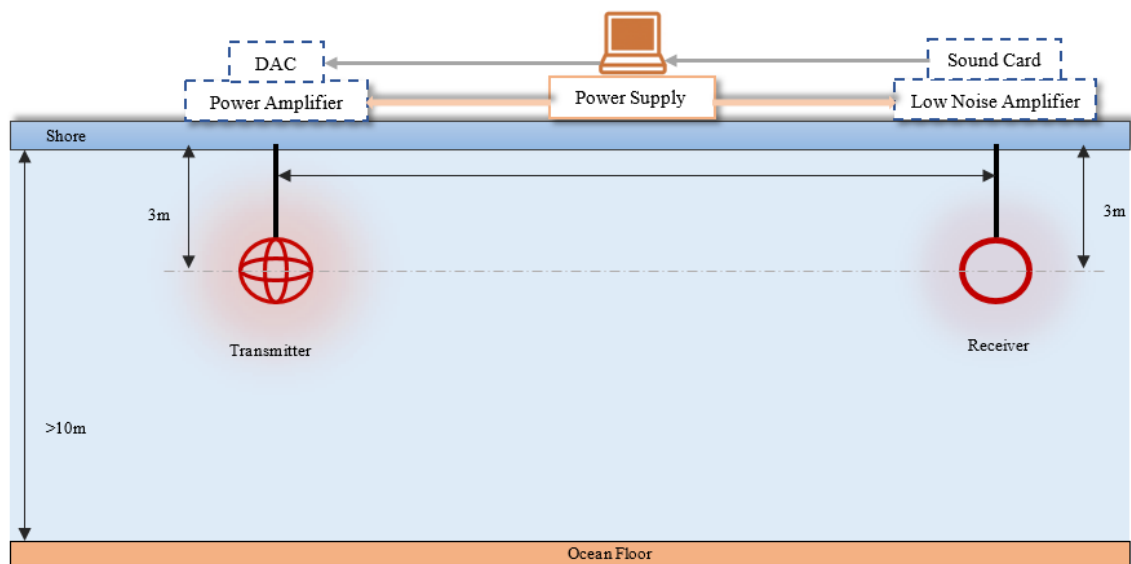


Figure 27: Schematic layout for underwater testing

Experiments were conducted in Dalhousie's Aquatron test tank to validate the path loss by conducting a measurement analysis in a circular seawater tank with a diameter of 15 meters and a depth of 3 meters. The conductivity of the water in the tank was measured to be equal to  $\sigma = 3.4\text{Sm}^{-1}$ .

Table 4: Aquatron Tank Facility Specifications

Diameter	15.24meters (50 feet)
Depth	3.5m perimeter – 3.9m center(app)
Volume	684,050litres
Materials	Steele reinforced concrete, Polyester and glass – fiber liner with an epoxy sealant
Water	Filtered sea water (33% salinity)
Bridge	Operation: Hydraulically controlled Height: Raised or lowered up to 2.5 of the scrubbers Limitation: Equipment weighing up to 80Kg can be carried at the extremists of the bridge
Electrical outlets	6 locations with 115V/220V sockets around the pool

Transmitter:

To measure the effective coupling between the transmitter and receiver coils, tones are transmitted at different frequencies between 250Hz to 10kHz, while the coil is immersed at a depth of 2.8 meters. The tones for the three channels are generated using MCC-DAQs' USB-3101FS data acquisition card. TI's TAS5630 300-W Class-D audio power amplifier is used to provide a high-power output and has a maximum frequency of 10kHz. Note that the maximum power is limited by the 2-A maximum current specified by the DC supply and the frequency limitation at the MCC DAQ's inbuilt software gave access to use

maximum of 10kHz and works in the audio range of 44.1kHz equally split to its 4-channel output. The table 4, below shows the complete components list used at the transmitter section describing its parts and functionalities.

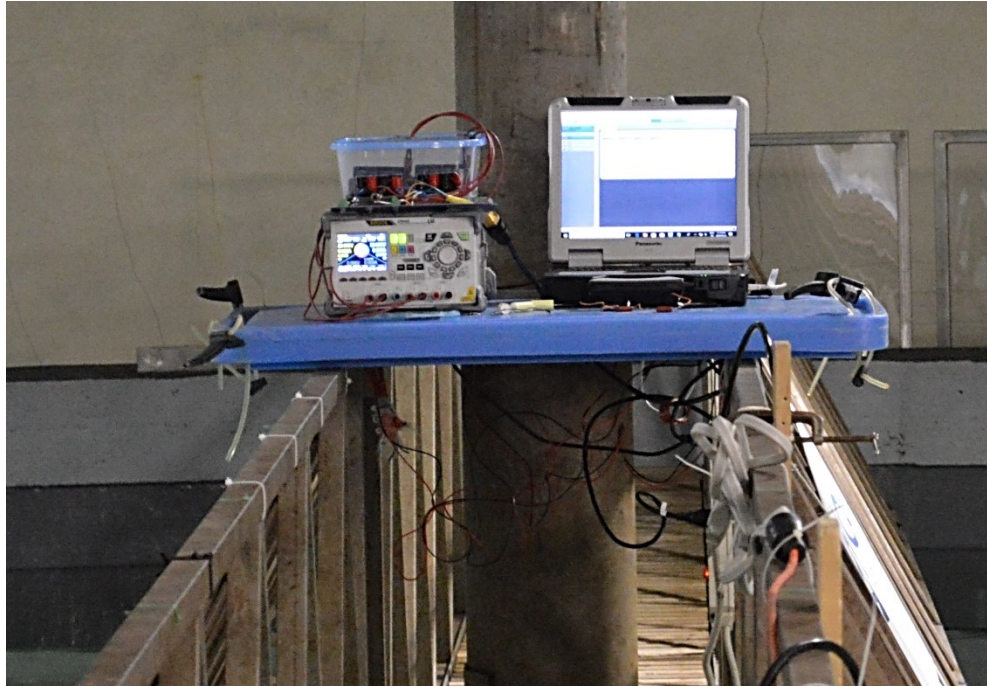


Figure 28: Transmitter signal processing set up

Voltage is supplied to the coil through the audio power amplifier. To limit the current, a resistance equal to  $R_{TX} = 10\Omega$  is placed in series with the resistance. To maintain a high, transmit current, a variable capacitance  $C_{var}$  is also added to the circuit to form a series RLC that resonates at the frequency of interest. Quality factor at the transmitter increases with frequency and its well below unity at 1 kHz.

$$Q = \frac{\omega L_{TX}}{R_{TX}} \quad (3.49)$$

As such, the variable capacitance is only added for test frequencies above 5kHz, when the impedance of the inductor is no longer negligible with respect to the resistance.

From class D power amplifier voltage supply across the coil is approximately,

$V_{TX} = 14 V_{PK}$  through the coil and the transmit current is

$$I_{TX} = \frac{V_{TX}}{R_{TX} + j\omega L_{TX} - \frac{j}{\omega C_{TX}}} \quad (3.50)$$

The choice of the carrier frequency has a significant influence on the transmission range and the coil number of turns provides an additional degree of freedom to control the system bandwidth.

The capacity of the MI link is shown in Figure 9 It can be observed that an optimum frequency exists to maximize the range for a given capacity. Below this frequency, the total path loss is dominated by coupling loss since the wavelength is much greater than the coil dimensions. In contrast, above the optimum frequency, the loss due to the conductivity in seawater becomes significant.

Table 5: Multi coil set up - Transmitter components list

<b>Transmitter parts</b>	<b>Description</b>
<i>Laptop</i>	Panasonic tough book - Instacal, DAQami software installed, LabVIEW interfaced as a back up
<i>USB -3101FS</i>	Measurement Computing data acquisition card (MCC-DAQ) – 4 channels  Audio Range of 44.1kHz with each 10kHz channel limitation
<i>Power Amplifier</i>	TAS5630PHD2EVM Class D type Evaluation Kit – to produce 3 channel output
<i>Power Supply</i>	RIGOL power supply calibrated $\pm 30V / 2.5A$
<i>Resistors</i>	10 $\Omega$ /20W resistor (3no's for each coil)
<i>Capacitors</i>	6.8uF 100Vdc (3-each for 5kHz – 8kHz)  2uF 400Vdc (3-each for 10kHz)
<i>MI loop coils</i>	3- circular loop coils ( <i>AWG-18</i> ) with 26 turns each  6cm,6.15cm and 6.25cm in radius respectively
<i>Measurement equipment</i>	Multimeter, Oscilloscope
<i>Accessories</i>	Cable assembly for transmitter fitted with wooden plank  3D printed Casings sealed with connector

## Receiver:

At the receiver, the circular coil is designed to have a radius  $a_{RX} = 6.25\text{cm}$  and its number of turns  $N_{RX}$  is equal to 26 turns. The receiver consists of a single coil differentially interfaced to an LT1167 low-noise amplifier (LNA) with  $100\ \Omega$  input resistance. For the LNA, two gain settings  $G_{LNA,1} = 97\ \text{V/V}$ , and  $G_{LNA,2} = 494\ \text{V/V}$  are defined to maintain linearity at short-range and reduce effect of noise at long-range. The output of the amplifier is applied to a sound card and recorded using Audacity for offline processing.

When the gear is fully submerged, the link power gain expressed by (2.34) can be measured between the transmitter and receiver. For this purpose, the receiver front-end gain between the input of the LNA and the output of the sound file must be characterized in advance. The table 5 below shows the complete components list used at the receiver section describing its parts and functionalities.



Figure 29: Transmitter and Receiver were deployed underwater

During the experiments, the receiver coil is normal to the  $y$ -axis shown in Figure 29 , and its height is carefully fixed to receive the maximum flux from the transmitter. During the

first experiments, transmitter *Coil 1* is facing the receiver coil and is expected to contribute most significantly to the flux at the receiver. The final experiment consists in evaluating the MI link gain as a function of angle in the *xy* plane. In this orientation, it is expected that the two coils oriented vertically will both contribute with different ratios to the flux at the receiver, while *Coil 3* will have negligible impact as it lies completely in the *z* plane.

Table 6: List of components used at the receiver section

<b>Receiver parts</b>	<b>Description</b>
<i>MI loop Coil</i>	Single circular Coil ( <i>AWG-18</i> ) with 26 turns and of 6.25 radius were hermetically sealed
<i>Low Noise Amplifier (LNA)</i>	Instrumentation Amplifier (LT1167) with different gain placed in a bread board  $G_{LNA, 1} = 97 \text{ app V/V}$ ,  $G_{LNA, 2} = 494 \text{ app V/V}$  Resistor selection for LNA gain, $R_G = 510\Omega, 120\Omega$ .
<i>External Sound Card</i>	Startech - USB Stereo Audio Adapter External sound card with SPDIF digital audio VT 1630A with volume handler and aux input
<i>Laptop</i>	Audacity3D software installed
<i>Power Supply</i>	RIGOL power supply calibrated $\pm 15V / 2A$
<i>Measurement equipment</i>	Multimeter, Oscilloscope
<i>Accessories</i>	6-m(Approx.) underwater Cable for receiver fitted with wooden plank

## 4.2 EXPERIMENTAL RESULTS

### 4.2.1 Noise Analysis

For the transmission of low-frequency magneto-inductive noise, it is important to consider the distribution of the atmospheric noise, since it is not considered to be white [20]. For this purpose, the noise power spectral density (PSD) is evaluated while the transmitter is silent. A long window  $n(t)$  spanning 10 seconds is recorded at the receiver at a sample rate of 44.1 kbps while the transmitter is silent. Assuming that the receiver total gain is  $G_{RX}$ , the noise PSD is calculated to be  $N_0 = \frac{PSD[n(t)]}{G_{RX}^2}$ . In *Figure 30*, the equivalent noise referred to the input of the LNA is shown. The noise PSD shown includes the atmospheric noise, ambient noise and contribution from the electronics. Note that for short ranges, the LNA gain is reduced to avoid nonlinearity. In these conditions, the noise floor is approximately 12 dB higher than that at the high gain setting shown in

*Figure 30*. As expected the noise PSD increases significantly at lower frequencies, and an inflexion point can be seen at approximately 10~kHz. This was also observed in [20].

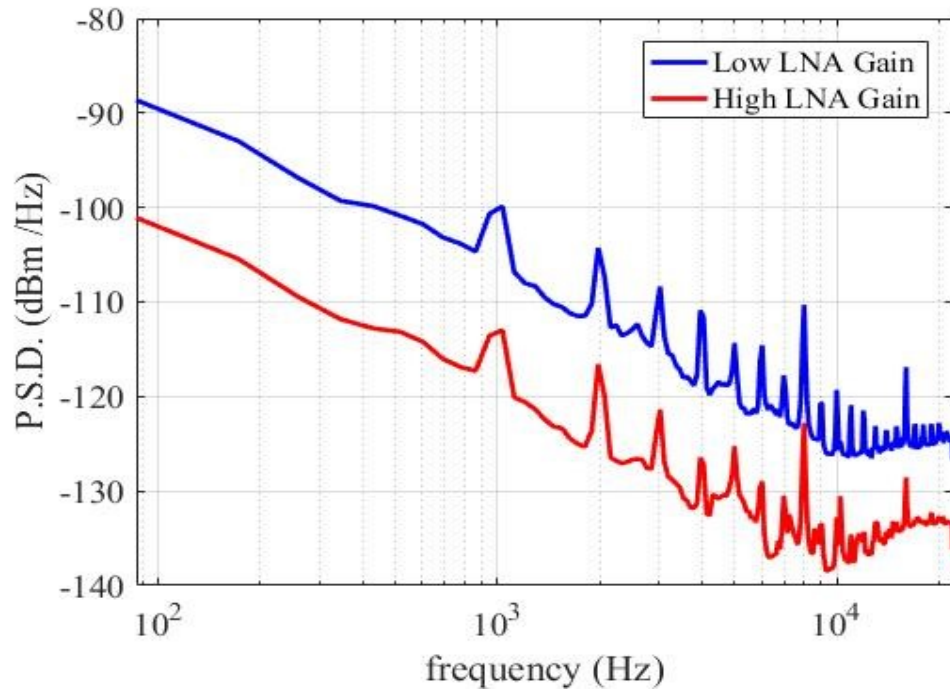


Figure 30: Measured noise at different gain levels

#### 4.2.2 Single Coil Response

The gain of the underwater MIC link is characterized for a single transmit coil facing the receiver coil to maximize the receiver flux. First the link gain is characterized at 2.8-meter depth. The measured path gain as a function of distance and frequency is represented in Figure 31. As predicted by the analytical models, the gain decreases with distance, and increases with frequency. For example, to achieve a -120 dB gain, at 1 kHz, the maximum distance is 2 meters. However, the same gain can be achieved using a 10 kHz frequency, but at a distance close to 4 meters. Note that for low frequencies, the measured received signal is within the noise floor of the receiver, such that the path gain becomes inaccurate.

In Figure 32, the path gain when the transmitter and receiver are submerged 2.8 meters below the surface is compared to that of the gain in air. As can be observed, the gain is only slightly greater in air by approximately 1 dB. This can be explained because the coil is only buried by a few meters below the sea surface, in comparison to the wavelength of the tone. Otherwise, using the definition of skin depth, the conductive losses are approximately 7 dB for a distance of 3 meters and at a 10 kHz frequency, which is much greater than what is measured.

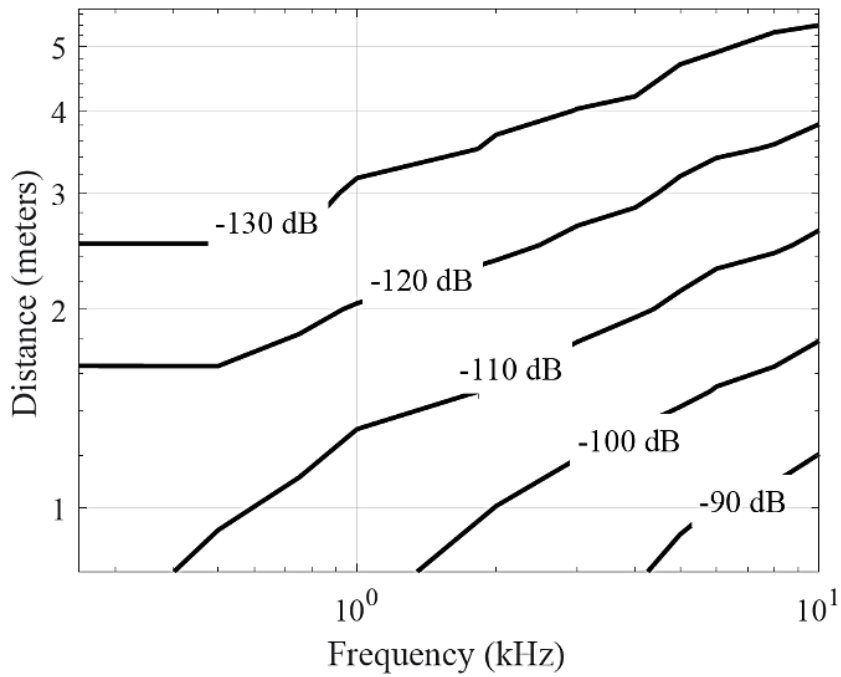


Figure 31: Measured Gain as a function of Frequency and Distance

Figure 33 shows the measured path gain as a function of frequency for different distances. The path gain is also compared to the predicted gain using equation (2.6) when the receiver does not resonate at the operating frequency. Note that the measured path gain is relatively close to the analytical value, particularly when the received signal power is above the noise floor, as characterized in Section 4.2.1.

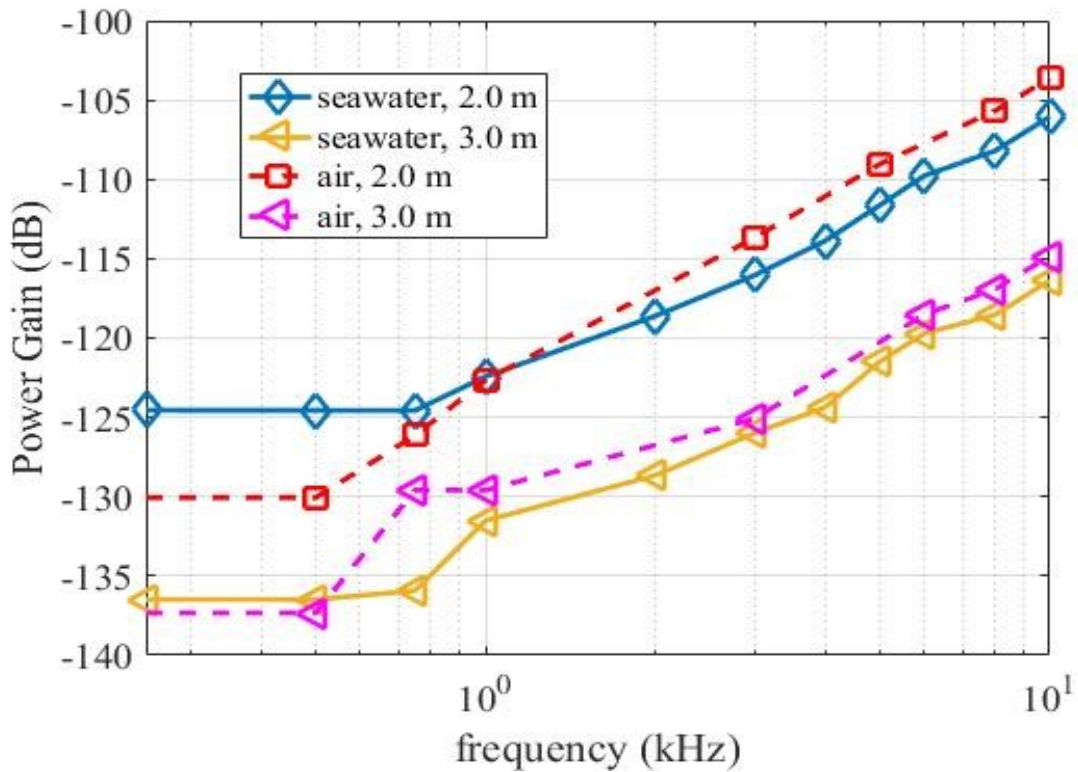


Figure 32: Comparison of Path Loss in Seawater and Air at 2m and 3m distances.

In

Figure 33, it can be observed that, in this low range of frequencies, to a first order approximation, the gain increases linearly with frequency. It is expected that the gain of

the link will start to decrease above the range of evaluated frequencies, particularly in deeper conditions. Also, the additional loss at low frequency can be reduced by adding a resonant capacitance at the receiver as predicted by equation (2.6).

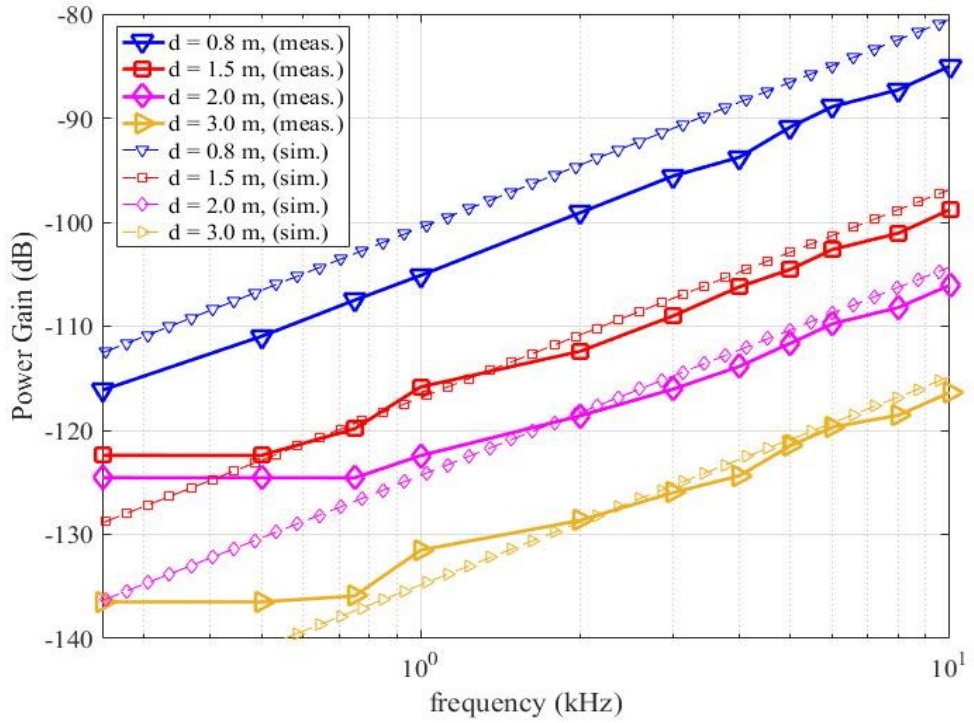


Figure 33: Comparison of Measured gain and Simulated gain as a function frequency for different distances

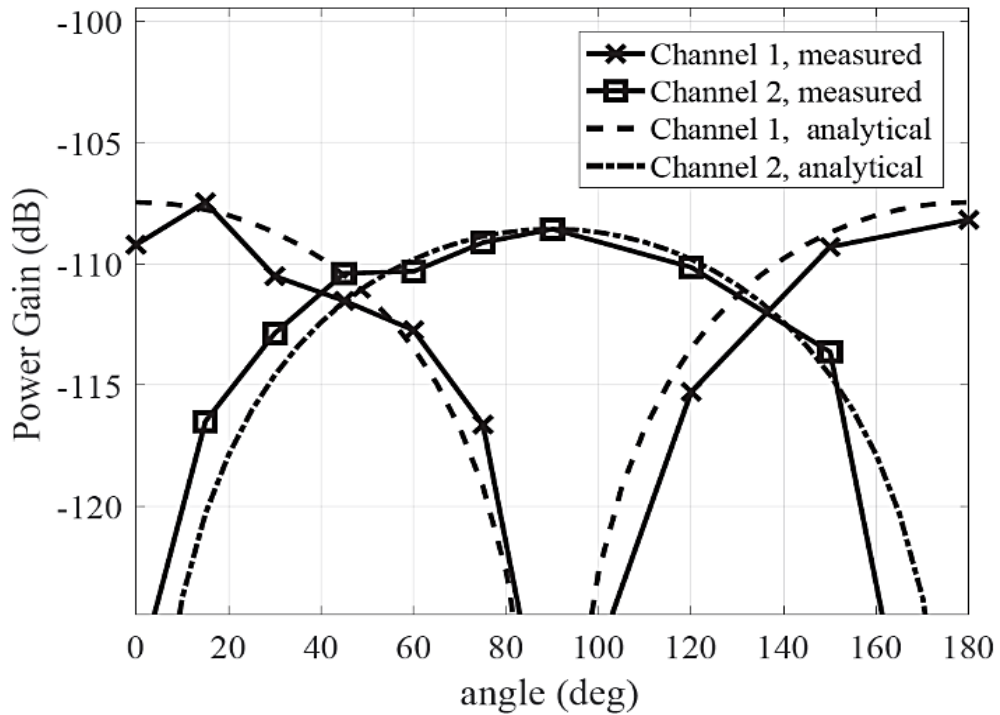


Figure 34: Comparison of Measured gain and Analytical gain as a function of Angle at 2meters distance for the multiple coil

#### 4.2.3 Multiple Coil Response:

In this section, the 3D coil path gain is assessed using the measurement results. During this test, the transmitter coil is rotated by 15 degrees, while the receiver is facing the transmitter from which it is separated by two meters. The power gain as a function of angle is shown in for the 3 different coils. Coil 1 and Coil 2 are the vertical coils, and as can be observed, Coil 1 obtains maximum gain when it is facing the receiver, while Coil 2 obtains a maximum gain at 90 degrees as expected. The third coil gain is much lower than for the two other channels, in fact it is more than 20 dB lower than the maximum gain obtain by the vertical coils. It can also be observed that by transmitting simultaneously from three

coils, the overall gain is much less sensitive to the transmitter angle. Specifically, the gain variation as a function of angle using 3 coils is approximately 10 dB, while the gain variation is over 20 dB using a single coil. This reduced variation can significantly improve the communication reliability of MI communications.

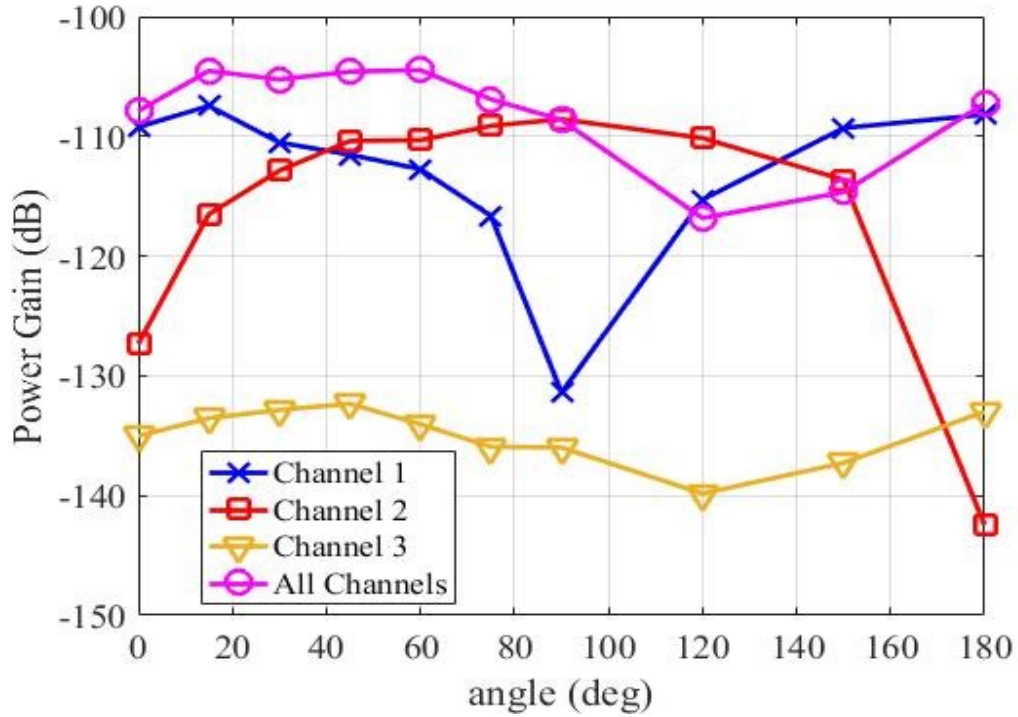


Figure 35: Pathloss as a Function of Angle for multiple channels

## CHAPTER 5 CONCLUSION

### 5.1 RESULTS

In conclusion, the expected capacity of a small-form factor low-power MI communication link is confirmed through measurements. Analytical simulations are used to predict a capacity on the order of 1 kbps for a maximum range of ~10meters and at an operating frequency approximately equal to 3 kHz.

A capacity of 100 kbps can also be achieved, but for a range of 4 meters. This model serves to extract the design constraints and its shown that for the specific coil design, an optimum frequency should remain in the low frequency band. By providing an improved matching network between the class D power amplifier set up and the transformer input will significantly improve the MI link.

The power gain of the MI link is also confirmed using measurements in a seawater tank. Since the measurements are accomplished in a shallow tank, the effect of conductivity in seawater is not fully appreciated. From the analysis we can say that the performance of the MI communication system in sea water is also good, although the path loss values are higher than in air and theoretically compared fresh water due to the electrical conductivity of sea water ( $\sigma \approx 3.4$ ). Nonetheless, the theoretical path gain using an untuned receiver is confirmed, and it can be expected that tuning the receiver will allow future implementations to approach the capacity of the link. The pathloss with MI communication is diminished with the coil radius and number of turns.

## **5.2 DISCUSSION ON FUTURE WORKS**

The various development and advancement in the future will prove the feasibility of MI communication in the Underwater Environment.

- To investigate whether a contactless wireless underwater coupling using 3-Orthogonal Coil for Underwater Wireless Sensor Network (UWSN)
- Demonstrate recharge time for the reusable battery focused on AUV docking station
- Adding multiple Receiver Coils/Relay coils to enhance the range for MI communication system
- Enhanced Diver Communications
- Future Internet of Underwater Things (IOUTs)

## APPENDIX A COILS COLOR SCHEMA



**Figure (14): Face View – SubConn 6 connector**

Inline cable/wire color	Inline cable number
Black	1
White	2
Red	3
Green	4
Orange	5
Blue	6

**Cable and Transmitter Coil matching:**

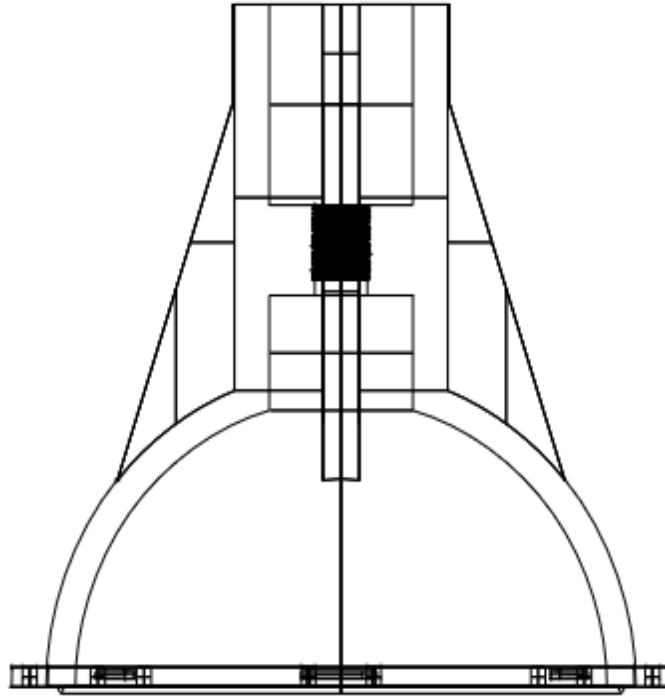
COIL Color	Inline Cable Number	Inline wire color
<b>Red Coil</b> <i>(Channel 1)</i>	<b>1</b>	<b>Red</b>
	<b>3</b>	<b>Black</b>
<b>Blue Coil</b> <i>(Channel 2)</i>	<b>2</b>	White
	<b>6</b>	<b>Blue</b>
<b>Green Coil</b> <i>(Channel 3)</i>	<b>4</b>	<b>Green</b>
	<b>5</b>	<b>Orange</b>

## APPENDIX B COIL ENCLOSURE DESIGN

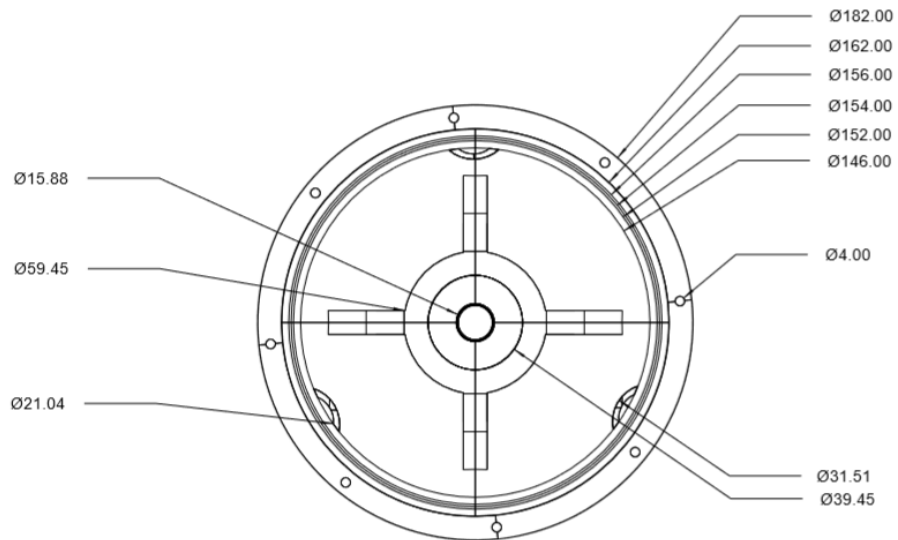
### Top Assembly:

*(all dimensions are in mm)*

Cross sectional View



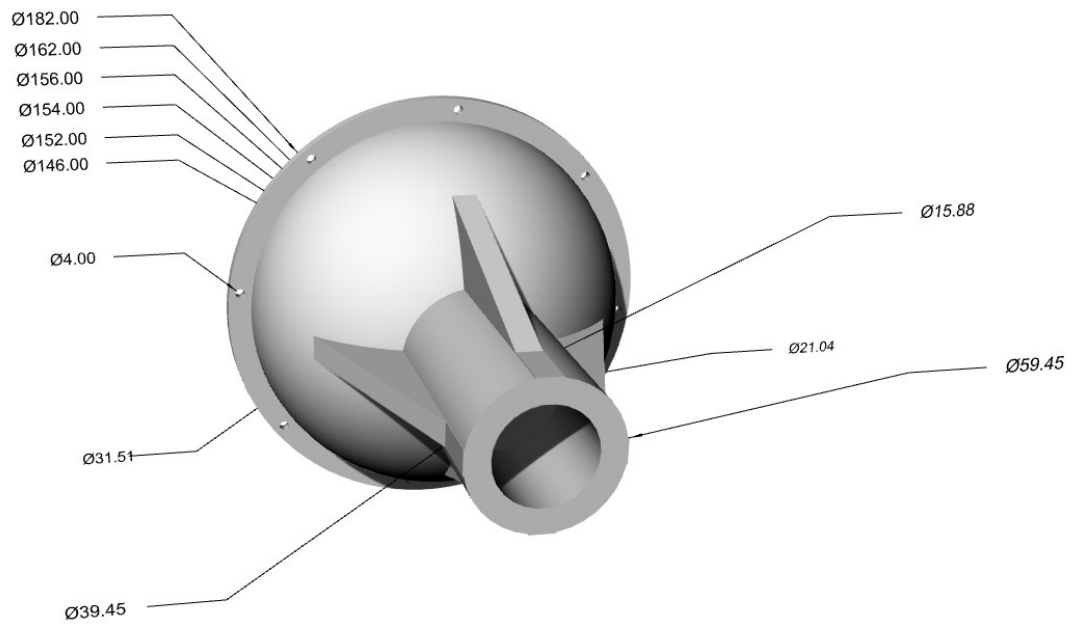
Bottom View



Sectional Sideview –from bottom



Sectional Sideview – from top



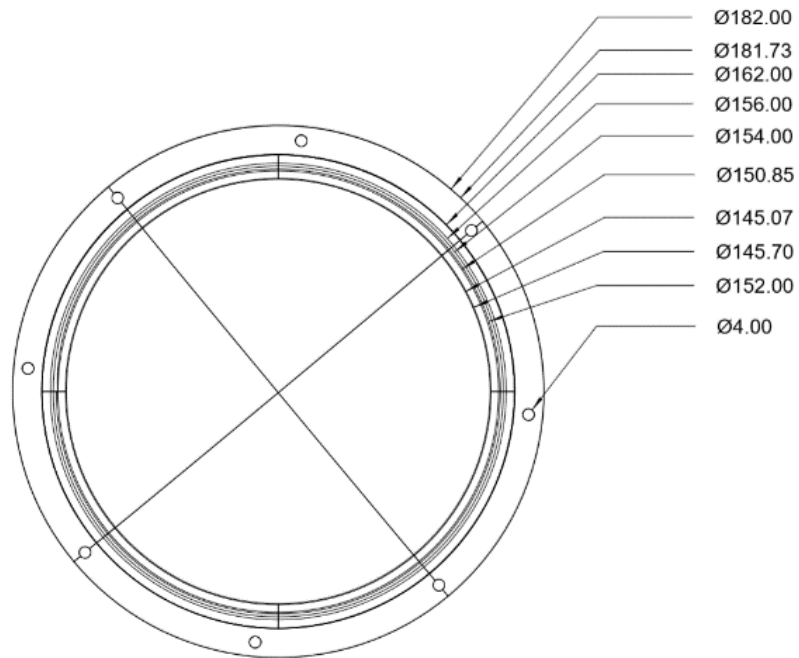
**Bottom Assembly:**

*(all dimensions are in mm)*

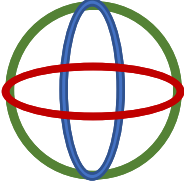
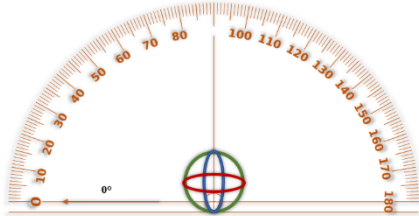
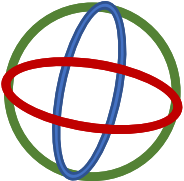
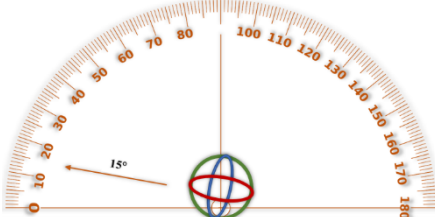
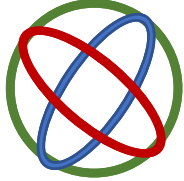
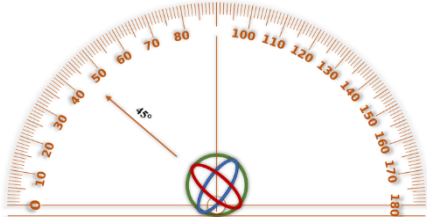
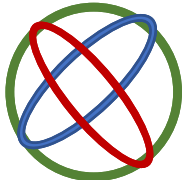
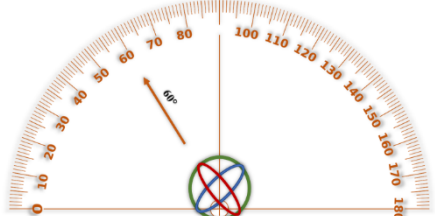
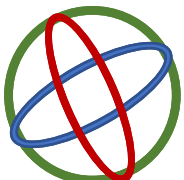
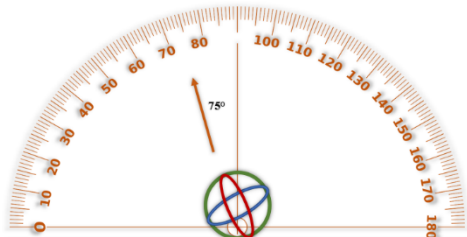
Cross sectional View:

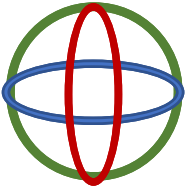
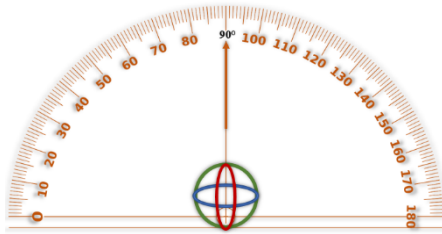
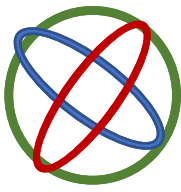
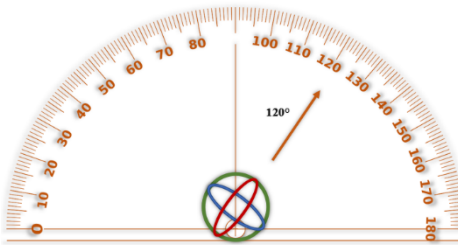
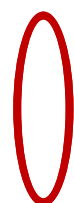
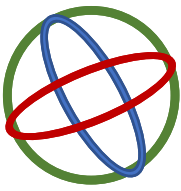
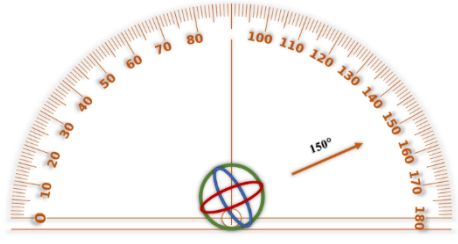
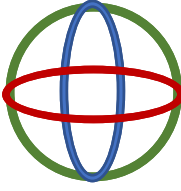
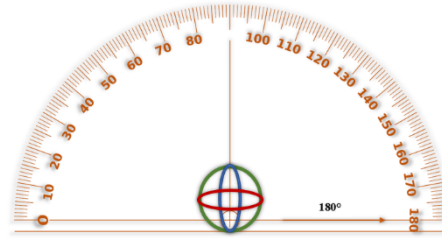


Top View:



## APPENDIX C TRANSMITTER BEAMFORMING ANGLES

Test angle	Transmitter Coil representation	Transmitter Coil and Angle orientation	Receiver Position
0°			
15°			
45°			
60°			
75°			

Test angle	Transmitter Coil representation	Transmitter Coil and Angle orientation	Receiver Position
90°			
120°			
150°			
180°			

## APPENDIX D DIGITAL MODEM

Prototype – Digital Modem using Atmel microcontroller

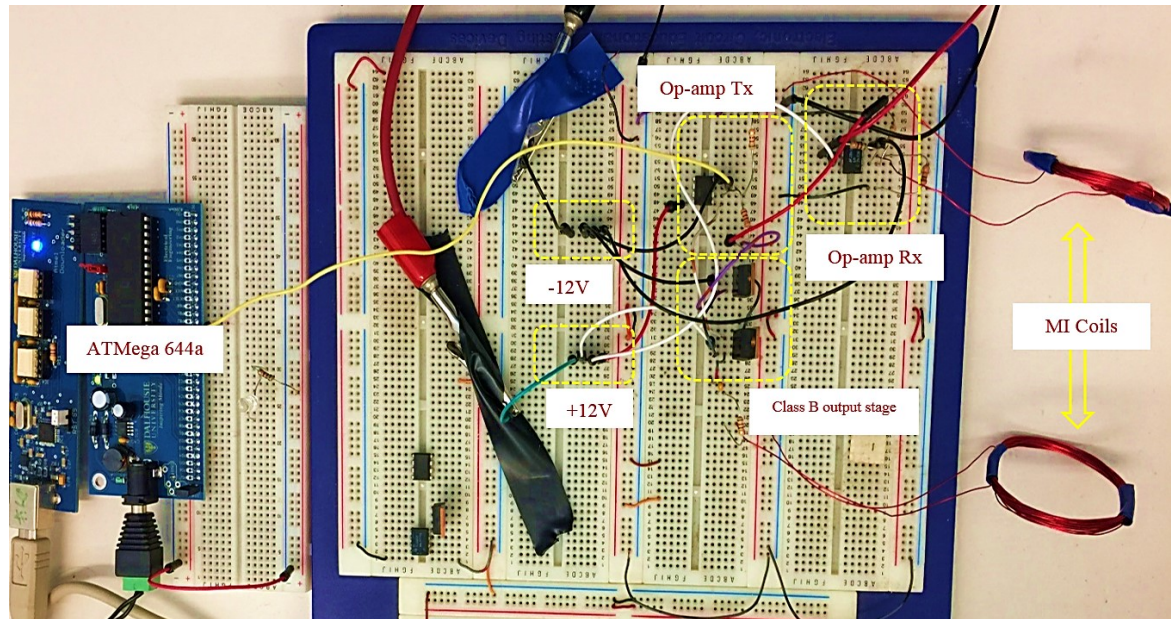


Figure: Implemented digital modem with Atmel microcontroller

Atmel Code

```
#include <avr/io.h>
#include <avr/interrupt.h>
#include <util/delay.h> // for switch delay function
volatile int counter_expired = 0;
int Cnt = 0;
/*****
This is the interrupt handler that is called every time the symbol
clock is expired
*****/
// TIMER1 overflow interrupt, called when TCNT1 overflows

ISR(TIMER1_COMPA_vect) // should it be TIMER0 or TIMER1 (this might be
your choice)
{
    counter_expired = 1;
    PORTC = Cnt++;
}
```

```

}
/*****
Initializing interrupt for timer1
*****/
void timer1_init()
{
    Cnt = 0;
    //to set my prescale 8
    TCCR1B |= (1<<WGM12) | (1<<CS11);
    TCNT1 = 0; // initialize my counter

    TIMSK1 |= (1<<OCIE1A); // overflow to enable // to be replaced
with OCIE1A

    TCCR1A = (1<<COM1A0);
    //TCCR1B |= (1<<WGM12);
    OCR1A = 918; //1KHz

    sei(); //enable global interrupt
}
/*****
Function to send data
*****/
void send_data(short frame_data, unsigned int current_data_idx)
{
    DDRB = (1<<PB3); // Set OC0 pin on PORTB for output
    // CTC Mode, Pre-scale 1/8
    TCCR0A = (1<<WGM01) | (1<<COM0A0);
    TCCR0B = (1<<CS01); //|(1<<CS00) ;// prescalar 8
    // enable transmit clock at X kHz on PB3
    if (frame_data & (1<< current_data_idx)) {
        TCNT0 = 0; // reset Counter
        OCR0A = 23; // 40 Khz
    }
    else{ // enable transmit clock at Y kHz

        TCNT0 = 0; // Zero Counter
        OCR0A = 31 ;// 30 Khz
    }
}
/*****
Function to send data, called by interrupt handler??
*****/
int main(void)
{
    DDRA |= (1<<PA0); //first pin of PORTA as Output

```

```

        // DDRA = 0x01;
        DDRD &= ~(1<<PD0); //firs pin of PORTD as Input
        // DDRD = 0x00; //all pins of PORTD input
while(1) //infinite loop
{
    if(PIND & (1<<PD0) == 1) //switch is pressed
    {
        PORTA |= (1<<PA0); //Turns ON LED
        _delay_ms(5000); //5 second delay
        PORTA &= ~(1<<PA0); //Turns OFF LED
    }
}

int is_frame_rdy = 1; // the frame is full and currently needs to
be sent
short frame_data = 0xAAAA; //sending 1010101010101010 - 8
rise\8falledges to detect
unsigned int current_data_idx = 1; // current index of the data
to be sent

// initialize the symbol counter to expire every 74msec
timer1_init();
DDRC = 0xFF; // to write

        //send_data(frame_data,
        current_data_idx++);
while (1)
{
    if(is_frame_rdy && (counter_expired == 1))
        // is symbol period expired during frame
        transmission
    {

        counter_expired = 0; // reset the expired flag to
false.

        if(current_data_idx < 17)
            send_data(frame_data, current_data_idx++);

        if(current_data_idx <= 16)
        {
            is_frame_rdy = 0;
            current_data_idx = 0;

            //TCCR0A &= ~(1<<COM0A0);
        }
    }
}
}
}

```

## BIBLIOGRAPHY

- [1] M. C. Domingo, "Magnetic Induction for Underwater Wireless Communication Networks," *IEEE Transactions on Antennas and Propagation*, pp. vol. 60, no. 6, pp. 2929-2939, June 2012.
- [2] N. Ahmed and Y. Rosa, "Magneto Inductive Communication System for Underwater Wireless Sensor Networks," Doctoral Thesis Proceedings, USA, 2017.
- [3] P. C. and H. Popenoe, "Diffuse high-bandwidth optical communications," in *OCEANS 2008*, Quebec City, 2008.
- [4] H. Kaushal and G. Kaddoum, "Underwater Optical Wireless Communication," *IEEE access*, vol. 4, pp. 1518-1547, 2016.
- [5] P. Pirinoli and Massaccesi, "Analysis of antennas for underwater applications," in *11th European Conference on Antennas and Propagation (EUCAP)*, Paris, 2017, pp. 1907-1910.
- [6] X. Che, I. Wells, G. Dickers, P. Kear and X. Gong, "Re-evaluation of RF electromagnetic communication in underwater sensor networks," *IEEE Communications Magazine*, Vols. vol. 48, no. 12., pp. pp. 143-151, December 2010.
- [7] S. Kisseleff, I. F. Akyildiz and W. Gerstacker, "Beamforming for Magnetic Induction based Wireless Power Transfer Systems with Multiple Receivers," in *IEEE*, USA, 2015.

- [8] M. Mallay, C. Touesnard and C. S, "Atmospheric Magnetic Noise Measurements in Urban Areas," in *IEEE Electromagnetics*, CA, 2014.
- [9] H. Guo and Z. Sun, "Increasing the Capacity of Magnetic Induction Communication Using MIMO Coil-Array," in *IEEE Global Communications Conference (GLOBECOM)*, Washington, DC, 2016, pp. 1-6.
- [10] N. Goding and J. F. Bousquet, "A compact magneto-inductive coil antenna design for underwater communications," in *WUWNET 17, ACM*, NY, USA, 2017, pp 19:1 - 19:5,.
- [11] Y. Wang, A. Dobbin and J. F. Bousquet, "A compact low-power underwater magneto-inductive modem," in *11th ACM International Conference on Underwater Networks & Systems*, Shanghai, China, Oct 2016.
- [12] H. Guo, Z. Sun and P. Wang, "Multiple Frequency Band Channel Modeling and Analysis for Magnetic Induction Communication in Practical Underwater Environments," *IEEE Transactions on Vehicular Technology*, Vols. vol. 66, no. 8, pp. pp. 6619-6632, Aug. 2017.
- [13] S. I. Babic, F. Sirois and C. Akyel, "Validity Check of Mutual Inductance Formulas for Circular Filaments with Lateral and Angular Misalignments," *Progress In Electromagnetics Research*, vol. Vol. 8, pp. 15-26, 2009.

- [14] S. Raghu, J. F. Bousquet and N. Chen, "Characterization of a 3D Underwater Magneto - Inductive Coil AArray," in *OCEANS 2018 MTS/IEEE*, Charleston,USA, 2018.
- [15] M. Ogihara and T. E, "Wireless Power and Data Transfer System for Station-Based Autonomous Underwater Vehicles," in *MTS*, 2015.
- [16] M. J and A. S, "Design and Development of Contactless Battery Charger for Underwater Vehicles," in *Michael Faraday IET International Summit(MFIIS2015)*, Kolkata,India, 2015, pp. 362-367.
- [17] N. W. Bergmann and J. Trevathan, "Wireless Underwater Power and Data Transfer," in *IEEE workshop, Sensor Network Application*, Australia, 2013.
- [18] D.Cheng, *Fundamentals of Engineering Mathematics*, Essex, England: Addison-Wesley & Co, 1993.
- [19] Y.Lee, "AN678: RFID Coil Design," *Tech. Rep Microchip*, 1998.
- [20] D.Gibson and W. A. David, "Channel characterisation and system design for sub surface communications," Lulu Enterprises, PhD thesis, University of Leeds, Leeds, Great Britian, 2003.
- [21] D. M. Pozar, *Microwave Engineering*, MA, USA: Wiley & Sons, 1998.
- [22] W. L. Stutzman and G. Thiele, *Antenna Theory and Design*, Wiley & Sons, 2012.

- [23] F. Akyildiz, P. Wang and Z. Sun, "Realizing underwater communication through magnetic induction," *IEEE Communications Magazine*, Vols. vol. 53, no. 11, pp. pp. 42-48, November 2015.
- [24] F. Campagnaro, F. Favaro, P. Casari and M. Zorzi, "On the feasibility of fully wireless remote control for underwater vehicles," in *48th Asilomar Conference on Signals, Systems and Computers*, Pacific Grove, CA, 2014, pp. 33-38.
- [25] O. Aboderin, L. M. Pessoa and H. M. Salgado, "Analysis of loop antenna with ground plane for underwater communications," in *OCEANS 2017*, Aberdeen,, 2017, pp. 1-6.
- [26] J. Nilson and S. Riedel, *Electric Circuits*, New Jersey, USA: Pearson Inc, 2012.
- [27] B. J. Heeres, "Contactless Underwater Power Delivery," in *IEEE*, 1994, P.418 - 423.
- [28] A. M. Bradley, "Power systems for AUVs," *IEEE journal of Oceanic Engineering*, pp. 526 - 538, 2001.
- [29] N. W. Bergmann and J. J., "Wireless Underwater Power and Data Transfer," in *Eight IEEE workshop - Building sensor network applications*, 2013, pp. 104-107.